Main Manuscript for

Molecular and isotopic evidence reveals the end-Triassic carbon isotope excursion is not from massive exogenous light carbon

Calum P. Fox[1,2,#], Xingqian Cui[3,4,#], Jessica H. Whiteside[5*], Paul E. Olsen[6*], Roger E. Summons[4], Kliti Grice[1*]

[1] Western Australia Organic & Isotope Geochemistry Centre, School of Earth and Planetary Sciences, Curtin University, Perth, Western Australia 6845.

[2] Department of Earth Sciences, Khalifa University of Science and Technology, PO Box 127788, Abu Dhabi, United Arab Emirates

[3] School of Oceanography, Shanghai Jiao Tong University, Shanghai 200030, China

[4] Department of Earth, Atmospheric and Planetary Sciences, Massachusetts Institute of Technology (MIT), 45 Carleton Street, Cambridge, MA 02139, USA

[5] Ocean and Earth Science, National Oceanography Centre Southampton, University of Southampton, Southampton SO14 3ZH, United Kingdom

[6] Department of Earth and Environmental Sciences, Lamont-Doherty Earth Observatory of Columbia University, 61 Route 9W, Palisades, NY 10964, USA

[#] These authors contributed equally to this work.

* Corresponding authors: Jessica H. Whiteside (J.whiteside@soton.ac.uk), Paul E. Olsen (polsen@ldeo.columbia.edu), Kliti Grice (K.Grice@curtin.edu.au).

Author Contributions: Conceptualization: C. P. Fox, J. H. Whiteside, P. E. Olsen, K. Grice; Formal Analysis: C. Fox, X. Cui, K. Grice, J. H. Whiteside, P. E. Olsen; Funding Acquisition: K. Grice, J. H. Whiteside, P. E. Olsen, R. E. Summons; Investigation: C. P. Fox, X. Cui; Resources: C. P. Fox, J. H. Whiteside, P. E. Olsen, K. Grice, R. E. Summons; Supervision: K. Grice, J. H. Whiteside; Visualization: C. P. Fox, X. Cui, J. H. Whiteside, P. E. Olsen, K. Grice; Writing: Original Draft: C. P Fox, K. Grice, J. H. Whiteside, P. E. Olsen; Writing review & Editing: C. P. Fox, J. H. Whiteside, P. E. Olsen, K. Grice, X. Cui, R. E. Summons.

This PDF file includes:

    Main Text
    Figures 1 to 4

Abstract (Words: 250)

The conventional interpretation of the negative organic carbon isotope excursion (CIE) associated with the end-Triassic mass extinction (ETE) as the result of a massive flux of isotopically light carbon into the ocean-atmosphere system from exogenous sources (e.g., thermogenic methane or CO_2 and/or methane clathrate dissociation linked to the emplacement of the Central Atlantic Magmatic Province (CAMP)), is contraindicated by new results from the CIE type locality. We demonstrate that a transition from marine to non-marine ecosystems in shallow-water environments in the Bristol Channel Basin, where the CIE was first described, was caused by an abrupt drop in relative sea level. Our new biomarker and compound-specific carbon isotopic data show that the emergence of microbial mats, influenced by an influx of fresh- to brackish-water, provided isotopically light carbon to both organic and inorganic carbon pools in cm-scale water depths, leading to the negative CIE. Thus, the iconic CIE and the disappearance of marine biota at the type locality are the result of local environmental change, and do not mark either the global extinction event or input of exogenous light carbon into the atmosphere. Instead, the main extinction phase occurs slightly later in marine strata, where it is coeval with terrestrial extinctions and ocean acidification driven by CAMP-induced increases in pCO_2; these effects should not be conflated with the CIE. An abrupt sea level fall observed in the Central European basins reflects the tectonic consequences of the initial CAMP emplacement, with broad implications for all extinction events related to large igneous provinces.

Significance Statement (Words: 120)

The end-Triassic mass extinction that occurred ~202 Myr ago is one of the "Big Five" biotic crises of the Phanerozoic Eon. It is also accompanied by an organic carbon isotopic excursion that has long been interpreted as the result of a global-scale carbon cycle disruption. Rather than being due to massive inputs of exogenous light carbon into the ocean-atmosphere system, the isotopic excursion is shown here to reflect regional sea-level change that caused a transition from a marine ecosystem to a less saline, shallow-water, microbial mat environment and resultant changes in the sources of organic matter. The mass extinction occurred slightly later, caused by abrupt injection of volcanogenic CO_2, is accompanied by only modest changes in organic carbon isotopic composition.

Main Text

Introduction

Most of the major mass extinctions of the last 300 million years, as well as some of the lesser biotic turnover events, are associated with reorganizations or perturbations of the Earth's carbon cycle, caused at least, in part, by massive inputs of carbon either sourced from or triggered by the emplacement of huge flood-basalt-dominated igneous provinces (1). The most aerially extensive of these magmatic systems, the Central Atlantic Magmatic Province (CAMP), has been tied (on land) by high-resolution geochronology to the ETE event at 201.6 Ma (2, 3). In marine environments, the unequivocal link between the ETE and the CAMP is far less direct, but the prevailing view is that the profound negative (>5‰ depletion in δ^{13}C) carbon isotopic excursion (CIE) associated with the ETE was caused by a massive input of exogenous, isotopically-light carbon to the ocean-atmosphere system from thermogenic and/or methane clathrate source(s), triggered by the initial phase of the CAMP. This dramatic CIE is often referred to as the "initial" CIE but herein, to avoid confusion, is named as the Bristol Channel Basin (BCB) CIE reflecting the area where this CIE was first observed (4). In order to constrain the source and timing of the end-Triassic isotopic shifts and to deconvolve this $\delta^{13}C_{org}$ excursion, we utilized organic biomarker and compound-specific isotopic techniques at one of the most extensively studied areas of the ETE, the BCB of southwest UK (Fig. 1). Our results indicate that the BCB CIE was a consequence of environmentally driven ecosystem changes in carbon sources due to regional sea level change, not the input of exogenous light carbon. Furthermore, the data suggest that the marine ETE occurred after this pronounced isotopic shift, in the latest Rhaetian, when massive inputs of CAMP-derived CO_2 caused ocean acidification, related environmental disruptions, and true global marine extinction. Consequently, the terminal Triassic CIE, although it may chronicle the initiation of the CAMP, is not directly associated with the ETE.

Geological and Environmental Context

The Bristol Channel Basin is a subdivision of the 1.8 million km^2 early Mesozoic Pangean Central European Basin. This basin was largely continental in the Norian (228 – 205.7 Ma), but by Rhaetian time in the Late Triassic (205.7 – 201.4 Ma) became an epicontinental sea with restricted circulation. Based on lithology and fossil evidence in the Westbury and Lilstock formations, the northern parts of this seaway (including the UK) had fluctuating salinity (5). Located on the northern flank of the CAMP (Fig. 1), the Central European Basin contains no lava flows or ash beds, hindering direct correlation with paroxysmal magmatic events. A well-documented cycle of sea level fall then rise throughout the basin occurred in the few hundred thousand years of the latest Rhaetian (6). It is within this environmental context that the BCB CIE, and its more southern correlatives, formed close in time to the ETE and initiation of the CAMP.

Results and Discussion

Sea level fall resulted in microbial mat emergence and ecological stress

Biomarker data for both the St. Audrie's Bay and Lilstock sections of the BCB (Fig. S1) suggest that the BCB CIE is a feature driven by ecological community changes forced by decreasing water depth and salinity within the basin, and by extension, to the European basin as a whole. We describe the biomarker results in stratigraphic (i.e., chronological) order below.

After an extended interval of predominantly non-marine red-bed deposition spanning most of the Triassic, the BCB was flooded by marine waters of abnormally low salinity, which deposited the dark mudstones of the Westbury Formation in the Rhaetian (5). Both sections show a relatively abrupt upward transition to the lighter-colored lower Cotham Member of the Lilstock Formation, characterized by fewer marine fossils and abundant oscillation ripples, indicating a shallowing water depth, but without much change in faunal composition. The lower Cotham and uppermost Westbury were subjected to folding and brecciation attributed, at least in part, to syn-depositional mega-seismic event(s) (7). Through the Westbury to Cotham lithological transition, perturbations in biomarker-inferred ecological and redox conditions are apparent. C_{30} steranes (24-*n*-propyl cholestanes; 24-npc), compounds derived from marine pelagophyte algae; show a constant decrease to zero (Fig. 2). Except for low diversity marine bivalves identified in the lower part of the Cotham Member in Lavernock Point, South Wales, a near absence in marine fossils throughout the Cotham Member supports a transition from a residual sea to a restricted shallowing non-marine environment (8, 9). Furthermore, declining values of the gammacerane index and ratios of isorenieratane/triaromatic steroids signify the termination of stratification (10) and disappearance of photic zone euxinia (PZE; a condition in which hydrogen sulfide is present in the sun-lit region of the water column) (11-14), respectively (Fig. 2). This is likely caused by the strong mixing of shallowing water that recharges oxygen throughout the water column. Additionally, strong shifts in the relative abundances of C_{27}, C_{28} and C_{29} steranes that generally represent red, chlorophyll-*c* containing, and green algae, respectively, are observed (SI; Fig. S2), implying an unstable environment sensitive to ambient perturbations, a common observation associated with shallowing water.

Truncating the folded lower Cotham seismite is an erosional surface downward from which intrude deep desiccation cracks (~>1 m), at which level the BCB CIE and the upper Cotham Member begins (Fig. 2). This sedimentological feature, as well as other evidence of desiccation with smaller crack length, wave ripples (Fig. 2), and possible rain drop imprints (8), indicates the CIE is recorded during maximum regression and cm-scale water depth (15). These upper Cotham Member mudstones vary in color from tan and red to light grey and have C_{30} sterane index values near zero, implying freshwater recharge. Both biomarkers and $\delta^{13}C_{org}$ values in the upper Cotham

Member shift in the position and magnitude within the CIE. Consequently, the CIE can be divided into two stages, the "lower CIE" and "upper CIE".

The lower CIE is characterized by large offsets in the timing and magnitude (~3 ‰) of $\delta^{13}C_{org}$ between the two sections, likely related to small differences in sedimentation rates (i.e., Lilstock encompasses the entire CIE and St. Audrie's Bay encompasses a variety of sedimentary rock types containing the excursion). Consistently low 3-methylhopane index values (3-MeH index; SI Appendix, Fig. S2), which represent minimal contributions from aerobic methanotrophs, and increases in 2-methylhopane index values (2-MeH index; Fig. 2) are also observed. Although 2-MeH is typically used as a biomarker for cyanobacteria, other organisms, exemplified by α-proteobacteria, have the capacity to produce 2-methyhopanoids (15, 16), preserved as 2-methylhopanes in sediments, complicating interpretations of the 2-MeH index in the geological record. Rather, studies suggest that modern marine cyanobacteria are minor producers of 2-methylhopanoids compared to other sources such as α-proteobacteria and plant-associated (i.e. soil, wood degradation), terrestrial and freshwater environments (17, 18). In the context of microbial systems, the modern Laguna Guerrero Negro (Baja California) hypersaline microbial mats and Highborne Cay stromatolites (Bahamas) show evidence of *hpnP* genes (required to produce 2-methylhopanoids) equally contributed by cyanobacteria and α-proteobacteria (17). Contrastingly, the pustular and smooth microbial mats in the hypersaline lagoon of Shark Bay, Western Australia show evidence of *hpnP* genes from a predominantly cyanobacterial source despite a major contribution of α-proteobacteria in the mats (19). Whether primarily sourced from cyanobacteria or α-proteobacteria, increases in the 2-MeH index in the lower CIE interval possibly constitute a microbial mat source. Additionally, a well-mixed water column at the lower CIE is evidenced by low gammacerane index values, consistent with tan- to red-colored mudstones. Chlorobactane and okenane, pigment-derived biomarkers for high-light-adapted anoxygenic phototrophic green-pigmented green and purple sulfur bacteria (GGSB and PSB) (12, 20), respectively, are barely detectable (SI Appendix, Fig. S8). Increasing relative abundances of low-light-adapted brown-pigmented GSB (BGSB), indicated by ratios of isorenieratane/triaromatic steroids are also observed (Fig. 2) (21, 22), however such increases are mostly an order of magnitude lower compared to those above and below the CIE. Altogether, these changes strongly argue for the initiation of freshening and shallowing conditions populated by thin, microbial mat communities containing oxygenic cyanobacteria and/or α-proteobacteria, and point to the dramatic perturbations to the ecosystem and environment at the lower CIE stage.

Nearly absent C_{30} steranes in the upper CIE, except one outlier sample, corroborate the interpretation of a non-marine environment throughout the Cotham Member. Another line of evidence is the elevated ratios of (renieratane and renierapurpurane)/isorenieratane [(ren+rnp)/iso] (Fig. 2). Renieratane and renierapurpurane are carotenoid biomarkers sourced from numerous strains of cyanobacteria (23, 24) and high (ren+rnp)/iso ratios, as observed in the upper CIE, are

typical of Phanerozoic lacustrine settings with low sulfate inventories (25). Increases in chlorobactane and okenane carotenoid biomarkers suggest expansion of anoxic green-pigmented GSB and PSB layers in microbial mats beneath surficial cyanobacterial layer(s) (Fig. 2). The co-occurrence of all these carotenoids requires redox stratification, a niche most parsimoniously attributed to a microbial mat source (21). Additionally, the gammacerane index increases in the upper CIE further support microbial mat formation and/or freshwater input. Although typically used as a stratification proxy in marine or hypersaline lagoon settings (10), increases of gammacerane in the upper CIE likely result from other source(s) of tetrahymanol (i.e., gammacerane precursor), such as phototrophic bacteria (26) and/or freshwater ciliates (27). Notably, many α-proteobacteria that produce 2-methylhopanoids also have the capacity to produce tetrahymanol, and an inverse relationship is observed between these compounds (16, 28). Thus, upper CIE gammacerane index increases are interpreted to be a direct response to ecological and environmental changes different to the lower CIE. Some of the largest and most dramatic changes in the relative abundances of the predominant C_{27}, C_{28} and C_{29} steranes and the ratio of algae to bacteria are also observed in the upper CIE at lowest $\delta^{13}C_{org}$ values (SI Appendix, Fig. S2). The oligotrophic and shallow water conditions of the upper Cotham Member support a habitat in which photosynthetic microbial mats could thrive alongside the observed generally oligohaline or freshwater biota (29), including darwinulid ostracodes, spinocaudatan crustaceans and the bryophyte *Naiadita lanceolata* (8, 30, 31).

The transition from the lower CIE to the upper CIE witnessed a significant reformation of the aquatic microbial community, with the upper CIE hosting the lowest $\delta^{13}C_{org}$ values (Figs. 2, 3). In addition, a principal component analysis (PCA) of the biomarkers interpreted to relate to a microbial mat source during the CIE (Fig. 2) reveals that most of the variability occurs during the upper CIE, and that 55 – 65% of variation can be explained in the first (PC-1) and second (PC-2) principal components (SI Appendix, text and Fig. S9).

The coeval Cotham Marble (covering 2000 km^2 elsewhere in the southwest UK) also contains the remains of microbial mat habitats during the CIE. Comprised of microbialites and laminar and thrombolytic stromatolites, this unit also displays a negative carbon isotopic profile (32, 33). Similar biomarkers have been attributed to microbial mats in the Chicxulub crater core that were transported from a carbonate platform by seiches and tsunamis after an asteroid impact (34). Accompanying the upper Cotham low-stand is the replacement of the marine biota by a non-marine flora and fauna (8, 31, 35). Though the extinction horizon is conventionally placed at this level at the CIE, the absence of marine Triassic taxa cannot be attributed to extinction because those taxa would be absent in the non-marine BCB even if the ETE never occurred.

Return to marine conditions

The termination of the CIE in the lower Langport Member is accompanied by a transgressive event that led to the re-establishment of a transitional marine environment, evidenced by a rise in C_{30} steranes and a return of the diagnostic carotenoid isorenieratane as the dominant photosynthetic pigment (Fig. 2). The synchronous responses in bulk isotope, C_{30} steranes, and other proxies (discussed later) strongly argue that the termination of the CIE is related to local depositional environment shifts (Fig. 2; SI Appendix, Fig. S2). For example, this boundary witnessed a rise in 2-MeH, sudden decline in freshwater ciliates and/or phototrophic bacteria (gammacerane index), elimination of aromatic carotenoid-producing cyanobacteria ([ren + rnp]/iso), resurgence of brown-pigmented GSB (isorenieratane/triaromatic steroids) (Fig. 2) and a strong methane cycle modulated by methanotrophs (3Me-H) (SI Appendix, Fig. S2). Additionally, minor perturbations in eukaryotic communities are observed based on C_{27-29} sterane compositions (SI Appendix, Fig. S2). Interestingly, C_{30} steranes anti-correlate with the relative density of cyanobacteria/ α-proteobacteria vs. aerobic methanotrophs (SI Appendix, Fig. S3), a relationship that is contrary to common observations, as summarized in (36). In our case, this pattern is most reasonably explained as reflecting the demise of the freshwater nitrogen-fixing cyanobacteria and/or α-proteobacteria present in microbial mats brought about by the marine transgression. Dynamic shifts in almost all biomarkers and PCA scores are observed in one sample of the Langport Member at Lilstock without significant change in $\delta^{13}C_{org}$ composition (Fig. 2; SI Appendix, Fig. S9). However, this interval is deposited within a heavily bioturbated level not observed at St. Audrie's Bay and is therefore considered a likely outlier. A shift back towards marine conditions in the middle to upper Langport Member is also indicated by a return of marine bivalve taxa, several of which disappeared at the base of the freshwater input at the CIE. Although several of these bivalve taxa persist into the overlying Blue Lias Formation, there are also several regional last appearances (37, 38). The uppermost mollusk-bearing Langport Member resembles the bioturbated marlstone and limestone facies that occur cyclically in the overlaying Blue Lias Formation, reflecting a return to fully marine conditions (Fig. 1). Conodonts occur for the first time in this unit, only to have their last occurrence in the overlying basal Blue Lias Formation (39), which also contains the last occurrence of the characteristic Late Triassic reptile clade Phytosauria (40).

The Langport Member to Blue Lias Formation transition, a previously debated flooding event (41, 42) corroborated here by the largest increase in the C_{30} sterane index (Fig. 2), is characterized by a negative shift in $\delta^{13}C_{org}$ and significant changes in biomarkers, including a switch from aerobic methanotrophy to cyanobacterial dominance and shifts in the proportions of C_{27} and C_{28} steranes (Fig. 2; SI Appendix, Fig. S2). The base of the Blue Lias Formation is marked by microlaminated organic matter rich mudstones ("paper shales"), the basal 2 cm of which contains a "Lilliput Assemblage" (43) of tiny (mm-scale) bivalves (SI Appendix, Fig. S4). The succeeding finely laminated 'paper' shales and remaining Pre-planorbis zone (lowermost Blue Lias Formation,

lacking ammonites, specifically *Psiloceras planorbis*) are characterized by a pronounced positive $\delta^{13}C_{org}$ shift (Fig. 1) (4) and numerous levels of abundant completely decalcified and poorly preserved bivalves of low diversity (SI Fig. S5), most simply interpreted as the results of a calcification crisis in which no aragonitic and few calcitic mollusks are preserved. Negative $\delta^{13}C_{org}$ values return with the re-appearance of ammonites, particularly *Psiloceras planorbis* that preserve the aragonitic nacre (Fig. 1). A marked microfloral swing with an acme of the conifer pollen form *Classopollis meyeriana* also occurs at the base of the Blue Lias Formation. The appearance of *Psiloceras planorbis* along with the sporomorph taxon *Cerebropollenites thiergartii* within the extensive *C. meyeriana* acme marks the approximate base of the Hettangian (44). Previously interpreted as a product of another major disruption in the exchangeable reservoirs between the terrestrial and marine realms at the ETE (4), and used as a chemostratigraphic marker (main CIE), this negative shift is now recognized as a change to long-term relatively negative $\delta^{13}C_{org}$ values lasting through the Hettangian Age, rather than a single event (42, 45).

Compound specific isotope analysis (CSIA) of the CIE supports its environmental origin

CSIA of biomarkers provides insight into how ecological change(s) contribute to the values of the $\delta^{13}C_{org}$ record. Synchronous isotopic shifts of biomarkers at the CIE onset and termination generally alludes to an exogenous ^{12}C source (Fig. 3; SI Appendix, Fig. S6). However, the myriad variations in biomarker $\delta^{13}C$ values and the extent of excursions at the CIE between the two sections (Fig. 3; SI Appendix, Table S1) does not support an exogenous ^{12}C source. Rather, the CIE reflects more complex endogenic origin(s) driven by ^{13}C-depleted carbon associated with microbial mats. Additionally, the low total organic carbon contents throughout the CIE (<1%; typically 0.2%) imply that only relatively minor changes in organic matter input would have pronounced significant effects on the $\delta^{13}C_{org}$ record. The following section describes in more detail differences between values of various biomarker isotopes and the $\delta^{13}C_{org}$ record, as well as the complex array of sources and related processes affecting $\delta^{13}C_{org}$ values.

Biomarkers investigated by CSIA include pristane and phytane typically derived from chlorophylls *a* and *b* (cyanobacteria and/or algae) (46), C_{17-19} *n*-alkanes from microbes including bacteria and algae (47), C_{23-25} odd-carbon-numbered *n*-alkanes from bryophytes (48) and other submergent plants (49, 50) and >C_{25} odd-carbon-numbered *n*-alkanes from land plants (51) (SI Appendix, Table S1).

Major differences in the biomarker $\delta^{13}C$ values observed between both sections occur at the onset of the CIE. For instance, at St. Audrie's Bay phytane exhibits the largest isotopic shift (-5.1‰) that seemingly mirrors an equal shift in the bulk $\delta^{13}C_{org}$ record, whereas at Lilstock, the largest compound-specific isotopic shifts are recorded in the C_{21-29} odd-numbered *n*-alkanes (-4.12

to -6.0‰), albeit lesser than the -8.1‰ bulk $\delta^{13}C_{org}$ excursion (Fig. 3; SI Appendix, Fig. S6 and Table S1). In addition, during the termination of the CIE at Lilstock, some of the largest isotopic shifts occur in the C_{21-29} odd-numbered n-alkanes with >5‰ positive shifts that are not mirrored in the bulk $\delta^{13}C_{org}$ record (3.6‰) (Fig. 3; SI Appendix, Fig. S6 and Table S1). Such discrepancies exemplify the CIE reflects a more complex, endogenic origin related to ecological change(s).

The covariation of $\delta^{13}C_{org}$ and $\delta^{13}C_{phytane}$ values through the CIE indicates that the CIE can primarily be explained by microbial community changes (Fig. 3). Specifically, within the CIE the most negative $\delta^{13}C_{org}$ values coincide with most negative $\delta^{13}C_{phytane}$ values (-34.8‰ and -33.9‰ at St. Audrie's Bay and Lilstock, respectively). Although pristane has its primary contributions from chlorophylls a and b in the water column, phytane has multiple predominant sources including cyanobacteria and methanogenic archaea residing in microbial mats as well as those from chlorophyll a and b containing photoautotrophic algae that reside in the water column. For example, phytane-related isoprenoids released after the cleavage of polar lipids have been detected in abundance in the hypersaline microbial mats of Shark Bay, Western Australia and Laguna Guerrero Negro, Mexico (52, 53). Originating from archaeol, such compounds are indicative of methanogens found in a range of environments including microbial mats (54-56). In algae n-alkyl lipids (e.g., C_{17-19} n-alkanes) are depleted in ^{13}C compared to the co-occurring isoprenoids by ~1.5‰, whereas in bacteria the opposite pattern is observed [(57) and references therein]. Based on increases in heterotrophy given by the positive isotopic offsets between n-alkanes (C_{17-19}) and isoprenoids (pristane and phytane) and the ~2‰ offsets between $\delta^{13}C_{pristane}$ and $\delta^{13}C_{pristane}$ during the CIE onset (Fig. 3), negative shifts in $\delta^{13}C_{phytane}$ are associated with increased bacterial activity of microbial mats. Enhanced preservation of phytane associated with microbial mat formation explains low CIE pristane/phytane ratios, typically associated with more reducing conditions (58), during red-bed oxic deposition (SI Appendix, Fig. S2). Therefore, the incongruity of the interpretation of redox conditions based on lithologic observation and biomarkers suggests that the Pr/Ph ratio is a source indicator associated with microbial mats rather than being simply an indicator of redox conditions (Fig. 2; SI Appendix, Fig. S2).

Microbial mats are known to produce lipids with greater ^{13}C-depletion compared to those of phytoplankton (59). Investigations into the isotopic composition of phospholipid fatty acids in modern freshwater microbialites have shown lipids greatly depleted in ^{13}C ($\delta^{13}C$ values ranging between -31.4±0.6 and 44.1±0.5‰) (60, 61) and biomarkers of sulfate-reducing bacteria (important contributors in microbial mat communities) in the carbonate matrix of concretions are also considerably ^{13}C-depleted ($\delta^{13}C$ values ranging between -40.5 and 42.0‰) (62). Furthermore, the recycling of ^{13}C-depleted autotrophic biomass by lower-residing heterotrophic layers within freshwater microbialites is required to explain changes in microbialite vertical $\delta^{13}C$ profiles and calcium carbonate precipitation equations whereby the local $\delta^{13}C_{DIC}$ becomes increasingly negative

as a result of microbial respiration (63, 64). Thus, the ^{13}C-depleted organic carbon associated with freshwater microbial mats and respiration-induced release of ^{13}C-depleted carbon to the inorganic carbon pool and its re-assimilation would be essential drivers of the CIE and possibly account for the minor offsets between the isotopic composition of pristane and phytane described above. Furthermore, methanogenic bacterial metabolism important in microbial mats produces methane in large quantities (29), meaning that microbial mat emergence in the SW UK could constitute an important methane source unrelated to the CAMP.

In the same interval at Lilstock, odd-numbered mid- to long-chain n-alkanes (C$_{21-27}$) show isotopic values more depleted than those of phytane, ranging between -34.8‰ and -36.3‰ (SI Appendix, Table S1 and Fig. S6). The ^{13}C-depleted mid-chain-length n-alkanes may be attributed to bryophytes and possibly other submerged/floating plants, as corroborated by fossil evidence that includes the aquatic bryophyte (liverworts) *Naiadita* and *Hepaticites* (along with freshwater to brackish Crustacea) in the Cotham Member (8, 31).The ^{13}C-depletion of long-chain n-alkanes with odd over even preference within the CIE has been cited as evidence of an input of light carbon into the atmosphere (65), based on data from Austrian sections. These sections, while having an overall similar lithostratigraphy (Fig. 1) and similar patterns in n-alkanes differ from those of the BCB in having high TOC values in the CIE. Furthermore, the longer chain n-alkane isotopic record fluctuates cyclically (66) through the St. Audrie's section (SI Appendix, Fig. S7) with more shifts in n-alkane than bulk organic δ^{13}C, an observation more parsimoniously explained by episodic floral changes tied to cyclical climate rather than multiple changes in atmospheric composition. Pollen and spore data from St. Audrie's Bay track mid- to long-chain n-alkane isotope values (Fig. 3; SI Appendix, Fig. S6 and Table S1) through the CIE (35). The CIE onset closely correlates with a greater abundance of pollen (dominated by *Classopollis meyeriana*) and terminates with a greater abundance of spores, the largest turnover in sporomorph taxa (Fig. 3). Spore-bearing plants such as lycophytes and monilophytes can exhibit higher carbon isotopic discrimination compared to pollen-bearing plants (e.g., gymnosperm and angiosperm) by up to ~ 5‰ in δ^{13}C values (67). Variation in plant inputs, although unlikely being the primary explanation of the CIE, most possibly is a consequence of local hydrologic/climatic shifts amplifying isotopic shifts, and contributing to the CIE (68). The shifts between autotrophic algae *vs.* heterotrophic bacteria together with cyclical land plant inputs (57, 69) during the CIE explain geochemical variations and differences, highlighting that local environmental changes triggered the onset and termination of the CIE, supporting that the CIE is endogenic in its origin.

Following the CIE, the δ^{13}C of pristane and phytane in the middle Langport Member are relatively constant and phytane is interpreted as being sourced largely from chlorophylls *a* and *b*. δ^{13}C values of the C$_{17}$ to C$_{19}$ and C$_{29}$ n-alkanes are generally more positive, with the exception of one negative excursion that has a negligible effect on the δ^{13}C$_{org}$ record, and is coincident with

pollen and spore changes and heavy bioturbation. Above this, across the upper Langport to Blue Lias transition, the δ^{13}C of pristane and phytane become relatively less stable, particularly at St. Audrie's Bay, and all *n*-alkanes, particularly C_{19} and C_{29}, show a negative excursion coincident with increases in *Classopollis* pollen and a negative shift in the $\delta^{13}C_{org}$ record (Fig. 3).

Revised relationship between the CIE and ETE

At the end-Triassic, extinction and isotopic events in multiple sections across Europe occur in different orders. In the BCB, the floral change occurs at the CIE prior to the last appearance of conodonts, whereas in the Austrian sections the floral changes occur after the CIE and the last appearance of conodonts (Fig. 1). Correlations between the last occurrence of conodont taxa in the UK and conodont extinction of the same taxa in Austrian sections suggests the lowermost Blue Lias Formation correlates to the *Choristoceras marshi* ammonite zone, which is largely regarded as occurring at the base of the marine extinction level (70). Recent work placed the UK marine extinction in the "dead zone" of the upper Cotham Member (37), however, this "dead zone" simply lacks marine invertebrates because it is a non-marine environment subjected to desiccation. The subsequent appearance of conodonts with the return of marine conditions suggest instead that the marine extinction level is at the base of the Blue Lias Formation. Here, the last phytosaurs (40) and conodonts (39), and low diversity, poorly preserved and decalcified marine taxa are due to one or more abrupt large increases in pCO_2 of CAMP origin. The negative $\delta^{13}C_{org}$ excursion at this level and the overlying positive $\delta^{13}C_{org}$ excursion might be a globally correlative marker (Fig. 1), more directly connected to exogenous carbon isotopic shifts related to the CAMP. This hypothesis may resolve the long-standing non-unique correlations deploying the CIE as the key event (66, 71, 72).

Biomarker and isotope data support the hypothesis that the CIE was caused by regional phenomena related to shallow-water microbial mats in a transient freshwater to brackish setting, as summarized in Fig. 4, rather than the CAMP-induced release of ^{13}C-depleted gasses such as methane. The organic carbon cycle changed in complex ways, with the CIE reflecting temporally, and to a lesser extent geographically, varying ecological changes, with concomitant isotopic shifts of differing magnitudes deposited during an interval of intense environmental change. By this hypothesis, the CIE was driven by microbial community changes and mat emergence because of regional relative sea-level fall and a shift from restricted marine to non-marine environments. Therefore, global chemostratigraphic correlations between the SW UK and other globally distributed sections must be revised. Many studied ETE sections with $\delta^{13}C_{org}$ records are from shallow marine to coastal environments in central European basins. As such, they too are potentially influenced by changing salinity and water depth. For example, in the Eiberg Basin, Austria, increases in the freshwater alga *Botryococcus* during the CIE may be responsible for the

large negative isotopic excursion in long-chain *n*-alkanes (73). It is noteworthy that in in fully continental sections, where $\delta^{13}C$ can be traced in the cuticle lipids of specific plant taxa, a negative CIE is not observed at the base of the extinction level (74).

The origin of the regional abrupt sea-level drop that allowed the development of shallow freshwater microbial mats at the CIE may be tied to the onset phase of the CAMP, which is now known to begin before the ETE (2). Plausible specific mechanisms include: 1) rising of hot asthenosphere causing doming of the crust and uplift of the European basins (75) or closure of marine gateways into the already restricted European basins, either or both of which would be predicted to cause transient sea level rise elsewhere; 2) eustatic sea-level drop if initiation of CAMP volcanism involved sustained SO_2 emissions, which could have led to the transient growth of glaciers (76). These hypotheses are consistent with our observations in the Bristol Channel and European basins. Confirmation must be sought through future ETE biomarker and compound-specific isotopic investigations in pelagic sequences that are not affected by changes in salinity and water depth, such as at Katsuyama, Japan (77), but which also have independent means of correlation such as magnetostratigraphy, U-Pb geochronology, and astrochronology.

Conclusions

Biomarker and compound-specific isotopic data from the Bristol Channel Basin at St. Audrie's Bay and Lilstock, UK show that the iconic CIE preceded the main ETE, and that the CIE itself is a record of freshwater microbial mat development and other ecological changes driven by a geologically transient, regional sea level change. Use of the BCB CIE and its European correlates as a global isochronous chemostratigraphic marker is therefore not tenable. The succeeding smaller negative isotopic excursion at the onset of the biocalcification event, associated with the last conodonts and the last phytosaurs, might be such a global isochronous marker. This interpretation of the CIE requires a re-analysis of global correlations at a tens-of-thousands-of-years resolution with independent correlation methods, and should lead to a better understanding of the regional *vs.* global effects of the CAMP on one of the largest mass extinctions in Earth history.

Materials and Methods

For $\delta^{13}C_{org}$ and total organic carbon (TOC) analyses, carbonates were removed from samples (dry weight <0.5g) by acid digestion and measured using a Delta V Plus mass spectrometer connected to a Thermo Flash 1112 via a Conflo IV and a CNHS elemental analyzer at the West Australian Biogeochemistry Centre, University of Western Australia. For biomarker analysis, bitumens were isolated from dry sediment samples (30-180g) by solvent extraction using a Milestone Start-E microwave extraction system in 50 mL of 9:1 dichloromethane:methanol (DCM:MeOH) using a

temperature program of 21 to 80°C over 10 minutes (held for 15 minutes). Elemental sulfur was removed using activated copper turnings and bitumen compounds were separated into saturate (*n*-hexane), aromatic (3:1 *n*-hexane:DCM) and polar (9:1 DCM:MeOH) fractions using column chromatography with activated silica gel. St. Audrie's Bay saturate fractions were analyzed using an Agilent 6890N gas chromatograph (GC) connected to a Micromass AutoSpec Ultima multiple reaction monitoring mass spectrometer (MRM-MS). St. Audrie's Bay aromatic and Lilstock combined saturate and aromatic fractions were analyzed using an Agilent 7890B GC connected to an Agilent 7010A triple quadrupole MS/MS. All GC-MRM-MS and GC-QQQ-MS analysis was conducted at the Summons Lab, Massachusetts Institute of Technology. Details on quality control regarding multiple instrument measurements are expanded in the supplementary file. Compound specific isotope analysis was conducted at Curtin University using a Thermo Trace GC Ultra connected to a Thermo Delta V Advantage isotope ratios MS (irMS) via a GC Isolink and Conflo IV. For full materials and methods please see the supplementary information.

References

1.   D. H. Rothman, Thresholds of catastrophe in the Earth system. *Science Advances* **3**, e1700906 (2017).

2.   J. Davies *et al.*, End-Triassic mass extinction started by intrusive CAMP activity. *Nature communications* **8**, 1-8 (2017).

3.   T. J. Blackburn *et al.*, Zircon U-Pb geochronology links the end-Triassic extinction with the Central Atlantic Magmatic Province. *Science* **340**, 941-945 (2013).

4.   S. P. Hesselbo, S. A. Robinson, F. Surlyk, S. Piasecki, Terrestrial and marine extinction at the Triassic-Jurassic boundary synchronized with major carbon-cycle perturbation: A link to initiation of massive volcanism? *Geology* **30**, 251-254 (2002).

5.   A. Swift, D. Martill, Stratigraphy (including biostratigraphy). *Fossils of the Rhaetian Penarth Group. The Palaeontological Association* **15**, 30 (1999).

6.   A. Hallam, The case for sea-level change as a dominant causal factor in mass extinction of marine invertebrates. *Philosophical Transactions of the Royal Society of London. B, Biological Sciences* **325**, 437-455 (1989).

7.   M. J. Simms, Uniquely extensive soft-sediment deformation in the Rhaetian of the UK: Evidence for earthquake or impact? *Palaeogeography, Palaeoclimatology, Palaeoecology* **244**, 407-423 (2007).

8.   M. Mayall, An earthquake origin for synsedimentary deformation in a late Triassic (Rhaetian) lagoonal sequence, southwest Britain. *Geological Magazine* **120**, 613-622 (1983).

9.   H. C. Ivimey-Cook, "The Permian and Triassic deposits of Wales" in The Upper Palaeozoic and Post-Palaeozoic Rocks of Wales*, T. R. Owen, Ed. (University of Wales Press, Cardiff, 1974), pp. 295-321.

10.   J. S. Sinninghe Damsté *et al.*, Evidence for gammacerane as an indicator of water column stratification. *Geochimica et Cosmochimica Acta* **59**, 1895-1900 (1995).

11.   J. A. Maresca, S. P. Romberger, D. A. Bryant, Isorenieratene biosynthesis in green sulfur bacteria requires the cooperative actions of two carotenoid cyclases. *Journal of bacteriology* **190**, 6384-6391 (2008).

12.   R. E. Summons, T. G. Powell, Chlorobiaceae in Palaeozoic seas revealed by biological markers, isotopes and geology. *Nature* **319**, 763-765 (1986).

13.   K. Grice, P. Schaeffer, L. Schwark, J. R. Maxwell, Molecular indicators of palaeoenvironmental conditions in an immature Permian shale (Kupferschiefer, Lower Rhine Basin, north-west Germany) from free and S-bound lipids. *Organic Geochemistry* **25**, 131-147 (1996).

14.   K. Grice, P. Schaeffer, L. Schwark, J. R. Maxwell, Changes in palaeoenvironmental conditions during deposition of the Permian Kupferschiefer (Lower Rhine Basin, northwest Germany) inferred from molecular and isotopic compositions of biomarker components. *Organic Geochemistry* **26**, 677-690 (1997).

15.   S. E. Rashby, A. L. Sessions, R. E. Summons, D. K. Newman, Biosynthesis of 2-methylbacteriohopanepolyols by an anoxygenic phototroph. *Proceedings of the National Academy of Sciences* **104**, 15099-15104 (2007).

16.   J. Ricci, A. Michel, D. Newman, Phylogenetic analysis of HpnP reveals the origin of 2‐methylhopanoid production in Alphaproteobacteria. *Geobiology* **13**, 267-277 (2015).

17.   J. N. Ricci *et al.*, Diverse capacity for 2-methylhopanoid production correlates with a specific ecological niche. *The ISME journal* **8**, 675-684 (2014).

18. J. Ricci, R. Morton, G. Kulkarni, M. Summers, D. Newman, Hopanoids play a role in stress tolerance and nutrient storage in the cyanobacterium Nostoc punctiforme. *Geobiology* **15**, 173-183 (2017).

19. T. J. Garby, M. R. Walter, A. W. Larkum, B. A. Neilan, Diversity of cyanobacterial biomarker genes from the stromatolites of Shark Bay, Western Australia. *Environmental microbiology* **15**, 1464-1475 (2013).

20. J. J. Brocks, P. Schaeffer, Okenane, a biomarker for purple sulfur bacteria (Chromatiaceae), and other new carotenoid derivatives from the 1640 Ma Barney Creek Formation. *Geochimica et Cosmochimica Acta* **72**, 1396-1414 (2008).

21. K. French, D. Rocher, J. Zumberge, R. Summons, Assessing the distribution of sedimentary C 40 carotenoids through time. *Geobiology* **13**, 139-151 (2015).

22. S. L. Jensen, Bacterial carotenoids. *Acta chem. scand* **19** (1965).

23. J. E. Graham, D. A. Bryant, The biosynthetic pathway for synechoxanthin, an aromatic carotenoid synthesized by the euryhaline, unicellular cyanobacterium Synechococcus sp. strain PCC 7002. *Journal of bacteriology* **190**, 7966-7974 (2008).

24. J. E. Graham, J. T. Lecomte, D. A. Bryant, Synechoxanthin, an aromatic C40 xanthophyll that is a major carotenoid in the cyanobacterium Synechococcus sp. PCC 7002. *Journal of natural products* **71**, 1647-1650 (2008).

25. X. Cui *et al.*, Niche expansion for phototrophic sulfur bacteria at the Proterozoic–Phanerozoic transition. *Proceedings of the National Academy of Sciences* **117**, 17599-17606 (2020).

26. G. Kleemann *et al.*, Tetrahymanol from the phototrophic bacterium Rhodopseudomonas palustris: first report of a gammacerane triterpene from a prokaryote. *Microbiology* **136**, 2551-2553 (1990).

27. F. B. Mallory, J. T. Gordon, R. L. Conner, The isolation of a pentacyclic triterpenoid alcohol from a protozoan. *Journal of the American Chemical Society* **85**, 1362-1363 (1963).

28. C. Neubauer *et al.*, Lipid remodeling in Rhodopseudomonas palustris TIE‑1 upon loss of hopanoids and hopanoid methylation. *Geobiology* **13**, 443-453 (2015).

29. C. M. Prieto-Barajas, E. Valencia-Cantero, G. Santoyo, Microbial mat ecosystems: structure types, functional diversity, and biotechnological application. *Electronic Journal of Biotechnology* **31**, 48-56 (2018).

30. W. S. Lacey, Fossil bryophytes. *Biological Reviews* **44**, 189-205 (1969).

31. E. Poole, The Triassic-Jurassic boundary in Great Britain. *Geological Magazine* **116**, 303-311 (1979).

32. Y. Ibarra, F. A. Corsetti, S. E. Greene, D. J. Bottjer, Microfacies of the Cotham marble: a tubestone carbonate microbialite from the Upper Triassic, southwestern UK. *Palaios* **29**, 1-15 (2014).

33. Y. Ibarra, F. A. Corsetti, S. E. Greene, D. J. Bottjer, A microbial carbonate response in synchrony with the end-Triassic mass extinction across the SW UK. *Scientific reports* **6**, 1-8 (2016).

34. B. Schaefer *et al.*, Microbial life in the nascent Chicxulub crater. *Geology* **48**, 328-332 (2020).

35. N. R. Bonis, M. Ruhl, W. M. Kürschner, Milankovitch-scale palynological turnover across the Triassic–Jurassic transition at St. Audrie's Bay, SW UK. *Journal of the Geological Society* **167**, 877-888 (2010).

36. K. L. French, J. E. Birdwell, M. V. Berg, Biomarker similarities between the saline lacustrine Eocene Green River and the Paleoproterozoic Barney Creek Formations. *Geochimica et Cosmochimica Acta* **274**, 228-245 (2020).

37. L. Mander, R. J. Twitchett, M. J. Benton, Palaeoecology of the Late Triassic extinction event in the SW UK. *Journal of the Geological Society* **165**, 319-332 (2008).

38. P. B. Wignall, D. P. Bond, The end-Triassic and Early Jurassic mass extinction records in the British Isles. *Proceedings of the Geologists' Association* **119**, 73-84 (2008).

39. A. Swift, First records of conodonts from the Late Triassic of Britain. *Palaeontology* **32**, 325-333 (1989).

40. M. W. Maisch, M. Kapitzke, A presumably marine phytosaur (Reptilia: Archosauria) from the pre-planorbis beds (Hettangian) of England. *Neues Jahrbuch für Geologie und Paläontologie-Abhandlungen* **257**, 373-379 (2010).

41. T. Hallam, P. Wignall, S. P. Hesselbo, S. A. Robinson, F. Surlyk, Discussion on sea-level change and facies development across potential Triassic–Jurassic boundary horizons, SW Britain. *Journal of the Geological Society* **161**, 1053-1056 (2004).

42. S. P. Hesselbo, S. A. Robinson, F. Surlyk, Sea-level change and facies development across potential Triassic–Jurassic boundary horizons, SW Britain. *Journal of the Geological Society* **161**, 365-379 (2004).

43. A. Urbanek, Biotic crises in the history of Upper Silurian graptoloids: a palaeobiological model. *Historical Biology* **7**, 29-50 (1993).

44. N. R. Bonis, M. Ruhl, W. M. Kürschner, Milankovitch-scale palynological turnover across the Triassic–Jurassic transition at St. Audrie's Bay, SW UK. *Journal of the Geological Society,* **167**, 877-888 (2010).

45. M. Ruhl *et al.*, Astronomical constraints on the duration of the early Jurassic Hettangian stage and recovery rates following the end-Triassic mass extinction (St Audrie's Bay/East Quantoxhead, UK). *Earth and Planetary Science Letters* **295**, 262-276 (2010).

46. T. Powell, D. McKirdy, Relationship between ratio of pristane to phytane, crude oil composition and geological environment in Australia. *Nature Physical Science* **243**, 37-39 (1973).

47. P. Cranwell, G. Eglinton, N. Robinson, Lipids of aquatic organisms as potential contributors to lacustrine sediments—II. *Organic Geochemistry* **11**, 513-527 (1987).

48. M. Baas, R. Pancost, B. van Geel, J. S. S. Damsté, A comparative study of lipids in Sphagnum species. *Organic Geochemistry* **31**, 535-541 (2000).

49. K. J. Ficken, B. Li, D. Swain, G. Eglinton, An n-alkane proxy for the sedimentary input of submerged/floating freshwater aquatic macrophytes. *Organic geochemistry* **31**, 745-749 (2000).

50. S. Tulipani, K. Grice, E. Krull, P. Greenwood, A. T. Revill, Salinity variations in the northern Coorong Lagoon, South Australia: Significant changes in the

ecosystem following human alteration to the natural water regime. *Organic geochemistry* **75**, 74-86 (2014).

51. G. Eglinton, A. Gonzalez, R. Hamilton, R. Raphael, Hydrocarbon constituents of the wax coatings of plant leaves: a taxonomic survey. *Phytochemistry* **1**, 89-102 (1962).

52. M. A. Allen, B. A. Neilan, B. P. Burns, L. L. Jahnke, R. E. Summons, Lipid biomarkers in Hamelin Pool microbial mats and stromatolites. *Organic Geochemistry* **41**, 1207-1218 (2010).

53. L. Jahnke *et al.*, Lipid biomarker and phylogenetic analyses to reveal archaeal biodiversity and distribution in hypersaline microbial mat and underlying sediment. *Geobiology* **6**, 394-410 (2008).

54. K. L. Lim, R. D. Pancost, E. R. Hornibrook, P. J. Maxfield, R. P. Evershed, Archaeol: an indicator of methanogenesis in water-saturated soils. *Archaea* **2012** (2012).

55. R. D. Pancost *et al.*, Archaeol as a methanogen biomarker in ombrotrophic bogs. *Organic Geochemistry* **42**, 1279-1287 (2011).

56. M. Sunamura, Y. Koga, K. Ohwada, Biomass measurement of methanogens in the sediments of Tokyo Bay using archaeol lipids. *Marine Biotechnology* **1**, 562-568 (1999).

57. K. Grice *et al.*, Photic zone euxinia during the Permian-Triassic superanoxic event. *Science* **307**, 706-709 (2005).

58. B. Didyk, B. Simoneit, S. t. Brassell, G. Eglinton, Organic geochemical indicators of palaeoenvironmental conditions of sedimentation. *Nature* **272**, 216-222 (1978).

59. G. A. Logan *et al.*, Terminal Proterozoic mid-shelf benthic microbial mats in the Centralian Superbasin and their environmental significance. *Geochimica et Cosmochimica Acta* **63**, 1345-1358 (1999).

60. A. Brady *et al.*, Photosynthetic isotope biosignatures in laminated micro-stromatolitic and non-laminated nodules associated with modern, freshwater microbialites in Pavilion Lake, BC. *Chemical Geology* **274**, 56-67 (2010).

61. R. A. White *et al.*, Biosignatures Associated with Freshwater Microbialites. *Life* **10**, 66 (2020).

62. I. Melendez *et al.*, Biomarkers reveal the role of photic zone euxinia in exceptional fossil preservation: An organic geochemical perspective. *Geology* **41**, 123-126 (2013).

63. M. Breitbart *et al.*, Metagenomic and stable isotopic analyses of modern freshwater microbialites in Cuatro Ciénegas, Mexico. *Environmental Microbiology* **11**, 16-34 (2009).

64. A. Nitti *et al.*, Spatially resolved genomic, stable isotopic, and lipid analyses of a modern freshwater microbialite from Cuatro Ciénegas, Mexico. *Astrobiology* **12**, 685-698 (2012).

65. M. Ruhl, N. R. Bonis, G.-J. Reichart, J. S. S. Damsté, W. M. Kürschner, Atmospheric carbon injection linked to end-Triassic mass extinction. *Science* **333**, 430-434 (2011).

66. J. H. Whiteside, P. E. Olsen, T. Eglinton, M. E. Brookfield, R. N. Sambrotto, Compound-specific carbon isotopes from Earth's largest flood basalt eruptions

directly linked to the end-Triassic mass extinction. *Proceedings of the National Academy of Sciences* **107**, 6721-6725 (2010).

67. A. S. Porter, C. Yiotis, I. P. Montañez, J. C. McElwain, Evolutionary differences in Δ13C detected between spore and seed bearing plants following exposure to a range of atmospheric O2: CO2 ratios; implications for paleoatmosphere reconstruction. *Geochimica et Cosmochimica Acta* **213**, 517-533 (2017).

68. K. H. Williford, K. Grice, A. Holman, J. C. McElwain, An organic record of terrestrial ecosystem collapse and recovery at the Triassic–Jurassic boundary in East Greenland. *Geochimica et Cosmochimica Acta* **127**, 251-263 (2014).

69. C. M. Jaraula *et al.*, Elevated pCO2 leading to Late Triassic extinction, persistent photic zone euxinia, and rising sea levels. *Geology* **41**, 955-958 (2013).

70. C. A. McRoberts, L. Krystyn, M. Hautmann, Macrofaunal response to the end-Triassic mass extinction in the West-Tethyan Kössen Basin, Austria. *Palaios* **27**, 607-616 (2012).

71. S. Lindström *et al.*, A new correlation of Triassic–Jurassic boundary successions in NW Europe, Nevada and Peru, and the Central Atlantic Magmatic Province: A time-line for the end-Triassic mass extinction. *Palaeogeography, Palaeoclimatology, Palaeoecology* **478**, 80-102 (2017).

72. J. A. Yager *et al.*, Duration of and decoupling between carbon isotope excursions during the end-Triassic mass extinction and Central Atlantic Magmatic Province emplacement. *Earth and Planetary Science Letters* **473**, 227-236 (2017).

73. A. Bachan, B. van de Schootbrugge, J. L. Payne, The end-Triassic negative δ13C excursion: a lithologic test. *Palaeogeography, Palaeoclimatology, Palaeoecology* **412**, 177-186 (2014).

74. K. L. Bacon, C. M. Belcher, S. P. Hesselbo, J. C. McElwain, The Triassic-Jurassic boundary carbon-isotope excursions expressed in taxonomically identified leaf cuticles. *Palaios* **26(8):461-9.** (2011).

75. A. Hallam, Z. E. Shaarawy, Salinity reduction of the end‐Triassic sea from the Alpine region into northwestern Europe. *Lethaia* **15**, 169-178 (1982).

76. B. Schoene, J. Guex, A. Bartolini, U. Schaltegger, T. J. Blackburn, Correlating the end-Triassic mass extinction and flood basalt volcanism at the 100 ka level. *Geology* **38**, 387-390 (2010).

77. W. Fujisaki *et al.*, Global perturbations of carbon cycle during the Triassic–Jurassic transition recorded in the mid-Panthalassa. *Earth and Planetary Science Letters* **500**, 105-116 (2018).

78. M. Ruhl, W. M. Kürschner, L. Krystyn, Triassic–Jurassic organic carbon isotope stratigraphy of key sections in the western Tethys realm (Austria). *Earth and Planetary Science Letters* **281**, 169-187 (2009).

79. A. v. Hillebrandt *et al.*, The global stratotype sections and point (GSSP) for the base of the Jurassic System at Kuhjoch (Karwendel Mountains, Northern Calcareous Alps, Tyrol, Austria). *Episodes* **36**, 162-198 (2013).

Figure Captions:

Figure 1: Critical events around the ETE in the Bristol Channel Basin (St. Audrie's Bay and Lilstock) and Austrian (Kuhjoch and Tiefengraben) areas. New St. Audrie's Bay and Lilstock $\delta^{13}C_{org}$ data are displayed in black and red, respectively. St. Audrie's Bay lithostratigraphy and extended $\delta^{13}C_{org}$ data (blue) are from ref. (4). Austrian lithostratigraphy and Kuhjoch $\delta^{13}C_{org}$ data (orange) are from ref. (78) and Tiefengraben $\delta^{13}C_{org}$ data (green) are from ref. (79). SW UK freshwater indicators are from ref. (8, 30, 31), bivalve extinctions are from ref. (37, 38), conodont extinctions are from ref. (39) and floral extinctions are from ref. (35). Austrian floral extinctions, conodont extinctions, ammonites, and freshwater indicators are after ref. (79). Note that the order of conodont and floral changes are reversed at the two areas, requiring the actual extinctions to occur simultaneously and later as shown by the ETE label. Ticks are at 1 meter intervals. Pangea reconstruction is based on ref. (4) including the lateral extent of CAMP (red). FO – first occurrence; LO – last occurrence.

Figure 2. Biomarker evidence of depositional facies changes at St. Audrie's Bay (● and solid lines) and Lilstock (■ and dashed lines) compared to the $\delta^{13}C_{org}$ and total organic carbon (TOC) records. The BCB CIE is displayed in light green (lower CIE) and pink (upper CIE), while newly proposed extinction onset is highlighted in light purple. The interpreted meaning of each biomarker-based proxy is indicated in bold above each column. Full details of the biomarker measurements are in the Supplementary Information. Principal component analysis (PCA) loosely represents an index of integrated variability corresponding to microbial mat formation, and represented here by principal component 2 (PC-2). Note that PCA was carried out for all samples except two samples from Blue Lias Formation, to avoid large bias introduced by the outliers and that the isorenieratane/triaromatic steroids is plotted in log scale. More information with regard to the comparison between PC-1 and PC-2 is expanded in the Supplementary Information. Formation abbreviations: BL – Blue Lias Formation; L – Langport Member; UC – Upper Cotham Member; LC – Lower Cotham Member; W – Westbury Formation. 2-MeH – 2-methylhopane; ren – renieratane; rnp – renierapurpurane; iso – isorenieratane; TA – triaromatic steroids; GGSB – high-light adapted green-pigmented green sulfur bacteria; PSB – purple sulfur bacteria; BGSB – low-light deep-water adapted brown-pigmented green sulfur bacteria.

Figure 3. Compound specific isotope analysis of pristane and phytane from St. Audrie's Bay and Lilstock, and n-alkanes from Lilstock. $\delta^{13}C_{17, 18, 19}$ indicates isotopic values of C_{17}, C_{18} and C_{19} n-alkanes displayed in different color intensities. Av. $\delta^{13}C_{(17, 18, 19)}$ – Av. $\delta^{13}C_{(pr, ph)}$ represents isotope mean value offsets between $C_{17,18,19}$ n-alkanes and pristane + phytane used to investigate autotrophy (auto) vs. heterotrophy (hetero). St. Audrie's Bay palynology data were previously reported from ref. (35) and are correlated here to Lilstock through lithological changes. The

inferred meaning of each compound is indicated in bold above each column. Formation abbreviations are given in Fig. 2.

Figure 4: Development of a microbial mat in the Bristol Channel Basin at the time of the terminal Triassic carbon isotopic excursion (CIE): 1, sea level regression resulting in subareal exposure and desiccation of the seabed, initiating the CIE; 2, formation of an oxic microbial mat with abundant cyanobacteria (oxygenic photosynthetic bacteria) under shallow, fresh-to-brackish-water; and 3, transition to an anoxic microbial mat with abundant Chromatiaceae (obligate anoxygenic phototrophic purple sulfur bacteria) and green pigmented Chlorobi (strict anoxygenic phototrophic green sulfur bacteria). Circular arrows in 2 and 3 indicate microbial mat-induced recycling of CO_2 and resultant ^{12}C enrichment, as discussed in text.
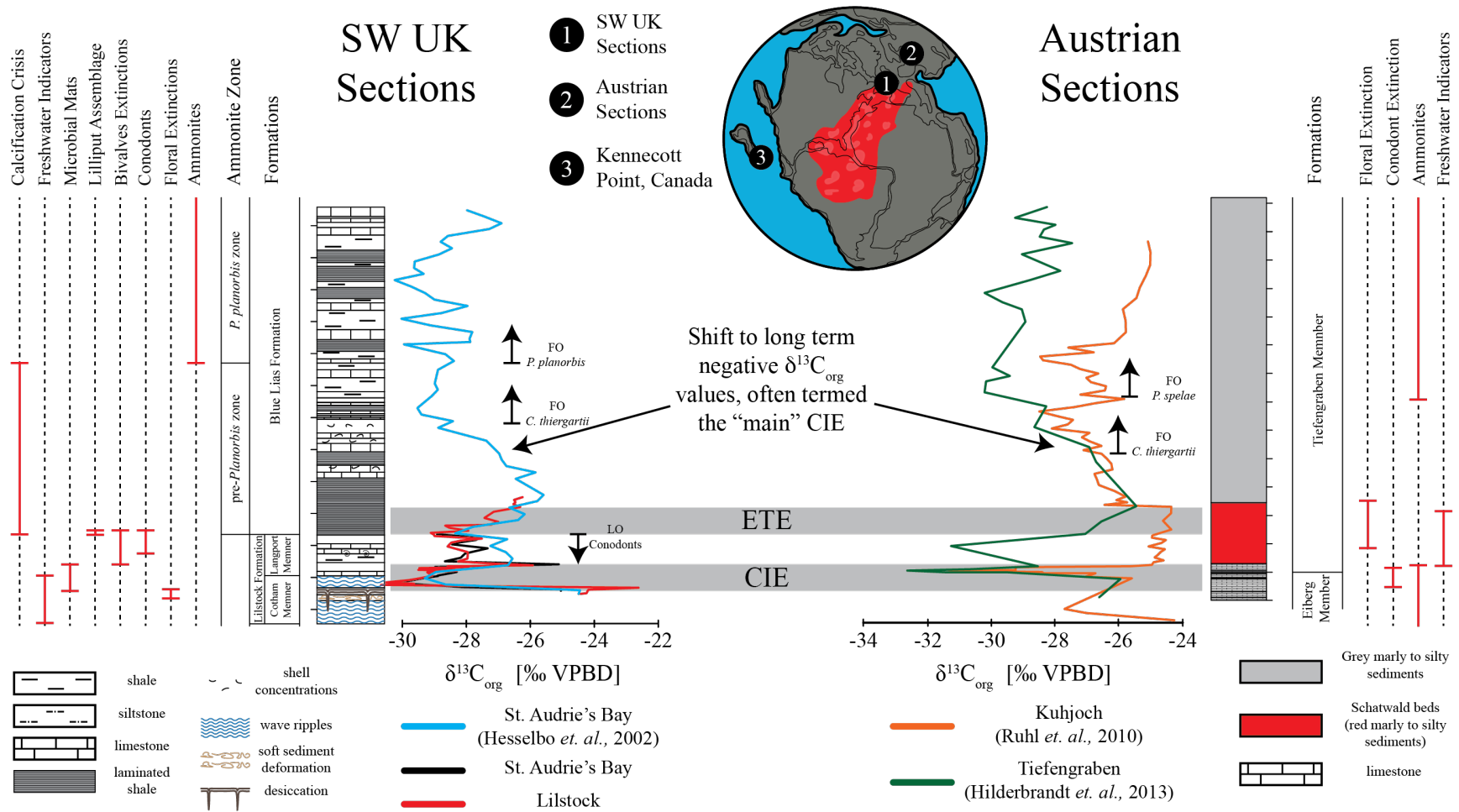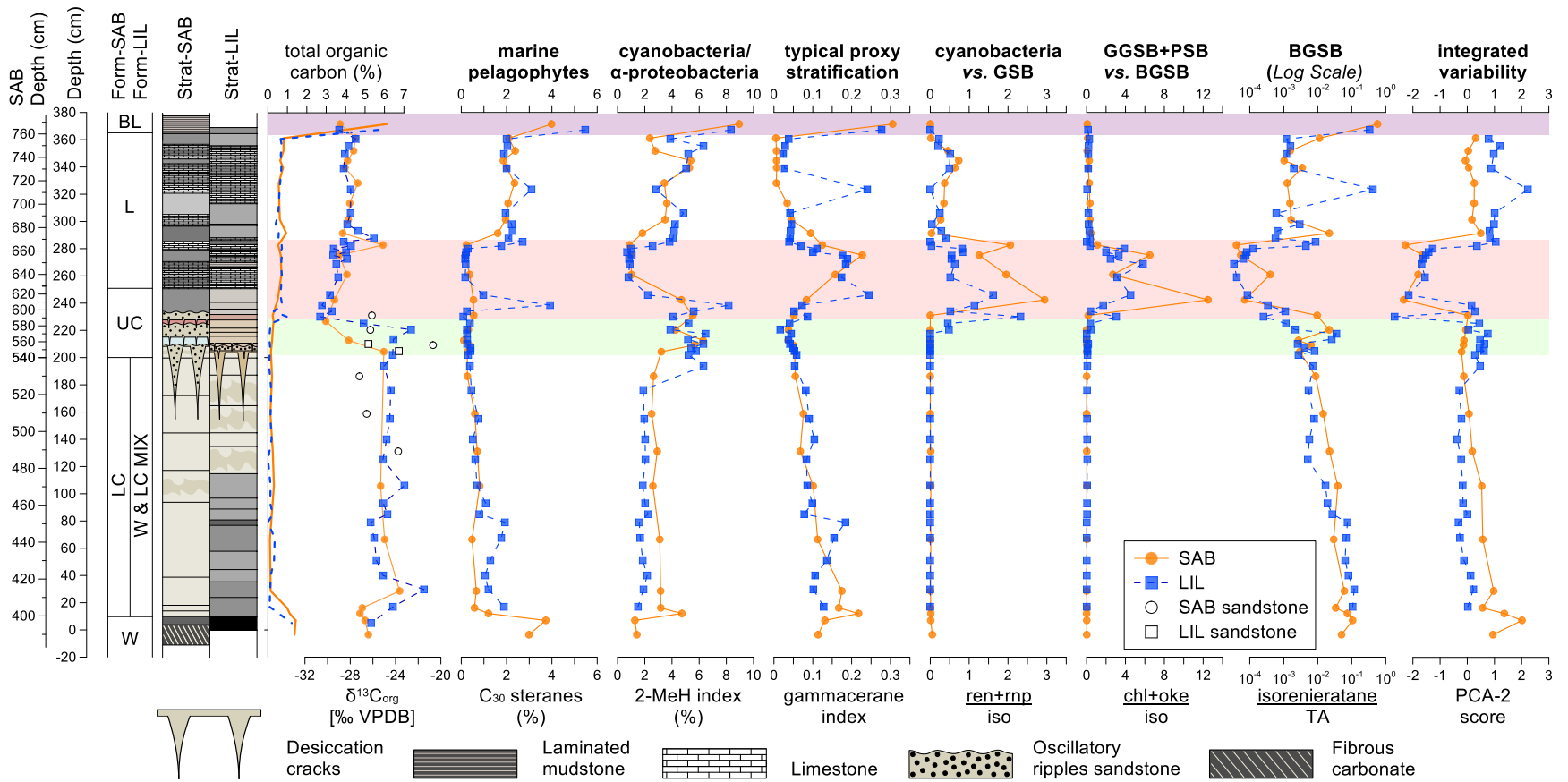
Figures and Tables

Figure 1
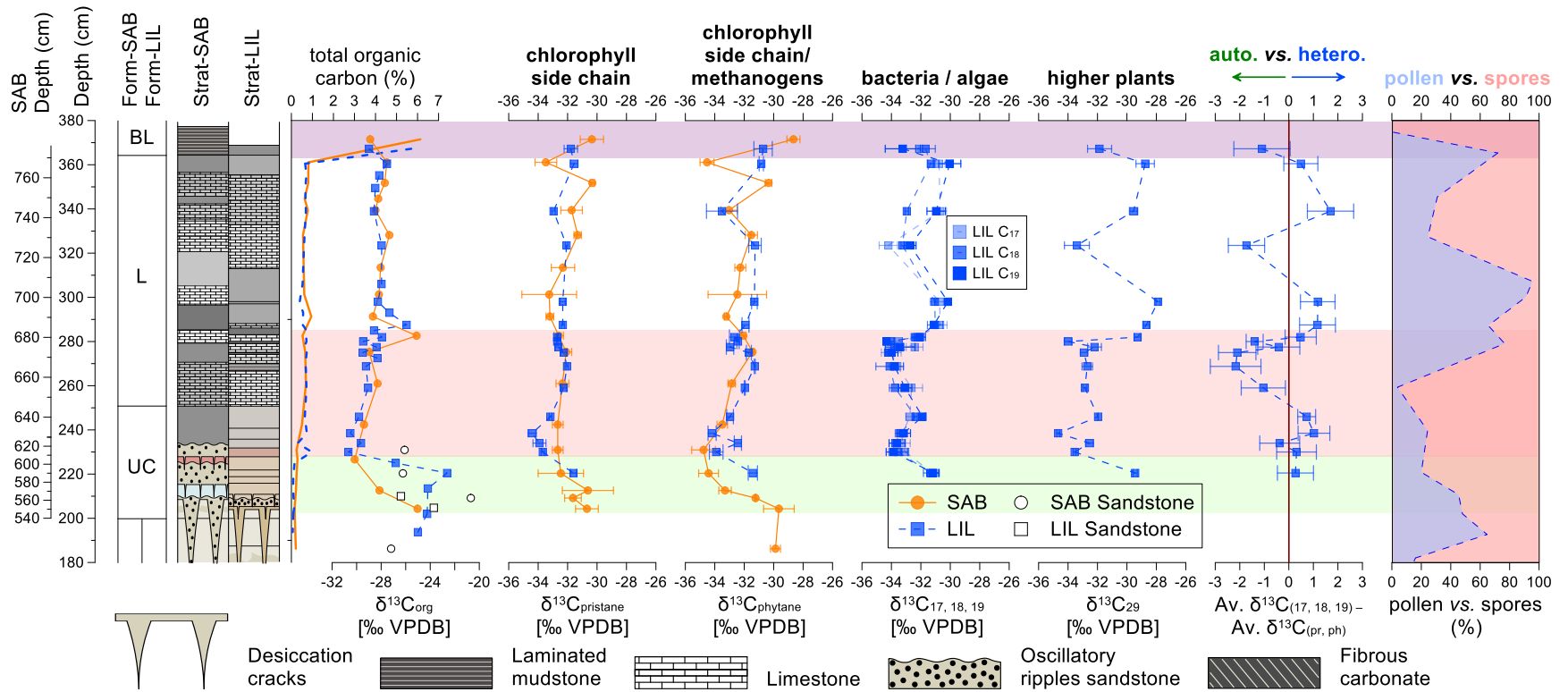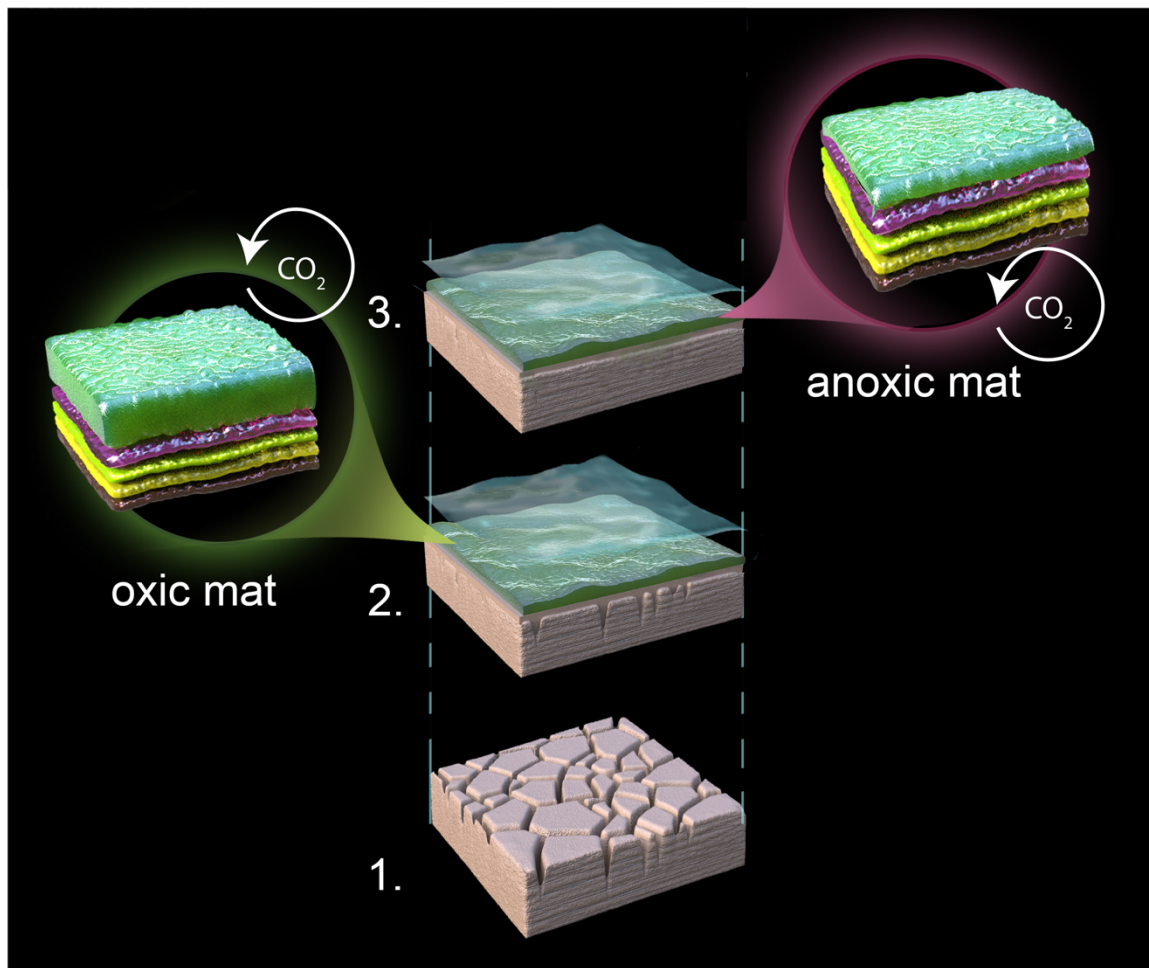
Figure 2

Figure 3

Figure 4

PNAS

www.pnas.org

Supplementary Information for

Molecular and isotopic evidence reveals the end-Triassic carbon isotope excursion is not from massive exogenous light carbon

Calum P. Fox, Xingqian Cui, Jessica H. Whiteside, Paul E. Olsen, Roger E. Summons, Kliti Grice

Paste corresponding authors names:

Email: polsen@ldeo.columbia.edu, J.Whiteside@soton.ac.uk, K.Grice@curtin.edu.au

This PDF file includes:

Supplementary text

Figures S1 to S8

Tables S1 to S2

SI References

Other supplementary materials for this manuscript include the following:

Datasets S1

St. Audrie's Bay and Lilstock Correlations

The lithological similarity between the St. Audrie's Bay and Lilstock sections allows correlation independent of palynology and geochemical proxies (Fig. S1). Correlations are based on the changing lithology type–sandstone filled desiccation cracks indicate the upper Cotham Member; a shift from Cotham Member grey/green mudstone to light and dark grey limestones signifies the upper Cotham Member to Langport Member transition; and the transition to highly lithified, high total organic carbon (TOC) black mudstones (shales) marks the Blue Lias Formation. Given the difference in thickness between the Lilstock and St. Audrie's Bay sections, the depth profile of St. Audrie's Bay is expanded such that the lithological transitions of the lower to upper Cotham Member, upper Cotham Member to Langport Member, and Langport Member to Blue Lias Formation all correlate at the same stratigraphic depth. Major differences in lithology between sections occur between the upper Cotham Member and Westbury Formation. At St. Audrie's Bay, this consists of the lower Cotham Member whereas at Lilstock this comprises a mix of the lower Cotham Member and Westbury Formation. Therefore, comparisons in biomarkers between sections during this interval may be more nuanced than in the overlying strata.

Biomarker indices, concentrations and origin

Many biomarker compounds of interest are presented as ratios. Typically, these indices are expressed as a ratio of one particular biomarker against one or more other compounds that are also present and which are typically less variable throughout the sequence and preferably not biased by instrumental factors. As such, these indices indicate relative, but not absolute abundances. Table S2 provides a summary of all these relationships and MRM precursor-product transitions used to detect the biomarker hydrocarbons used in this study.

The majority of biomarkers employed comprise steranes (largely derived from eukaryotic algae), hopanes (mostly derived from bacteria), triterpenoids (derived from plants and protists) and C_{40} carotenoids that act as accessory pigments. The most commonly measured steranes are those with 27 to 30 carbon atoms. The C_{27} steranes are indicative of red algae (1, 2), C_{28} steranes are typical of the chlorophyll a and *c* containing algae as well as some prasinophytes (3-5), C_{29} steranes are typical of other green algae and terrestrial plants (1, 5), and C_{30} steranes are representative of marine pelagophyte algae and, therefore, marine organic matter input (6). Due to some common ions in their mass spectra, signals from 4-methyl steranes can sometimes interfere with the signals from the C_{30} steranes when the abundances of the latter are low. Consequently, the C_{30} sterane index in this study has been calculated based only on the rearranged steranes (diasteranes) where this form of interference (or cross-talk) is minimal. Triaromatic steroids originate from algae but differ from the saturated sterane hydrocarbons in having different

diagenetic pathways. In this study triaromatic steroids are used for the normalization of aromatic carotenoids since: 1) total extracted lipids were fractionated into saturated/unsaturated and aromatic fractions; and 2) the saturated fractions of SAB samples were measured on the Waters Autospec under GC-MRM-MS mode, while the aromatic fractions were measured by Agilent GC-MS/MS. This change was necessitated when the former instrument ceased to function correctly. Therefore, the normalization of aromatic carotenoids against another group of major aromatic compounds was employed to minimize stratigraphic bias. For the purpose of quality control, two mixed oil standards (AGSO and GeoMark II) were measured on a Waters Autospec and Agilent GC-MS/MS in the same sequence with our samples. The instrument setup of the Agilent GC-MS/MS follows the role to best mimic chromatographic patterns acquired from the Waters Autospec. Therefore, results of saturated compounds acquired from the Waters Autospec and Agilent GC-MS/MS are comparable. Hopanes used in this study include the C_{30} $\alpha\beta$ hopane, C_{31-32} $\alpha\beta$ homohopanes, C_{30-32} 2α-methylhopanes and C_{30-32} 3β-methyhopanes. The latter two compound classes have been proposed as proxies for nitrogen-fixing cyanobacteria (7) and/or α-proteobacteria (8, 9) and aerobic methanotrophs (10-12), respectively. However, other organisms also contribute to the inventories of the 2- and 3-methylated hopanes and controls on the abundances of these compounds are still poorly understood. Gammacerane, thought to be primarily derived from tetrahymanol produced by ciliates, is typically used as a proxy for water column stratification (13), although other sources do exist as discussed in the main text. C_{40} carotenoids in this study are indicative of multiple phototrophic taxa. Purple sulfur bacteria (Chromatiaceae: PSB) are a known source of okenone, the precursor of okenane (14-16). Green-pigmented green sulfur bacteria (Chlorobi; GGSB) (17) require relatively high light intensities and are known to produce chlorobactene, the precursor of chlorobactane. In contrast, the closely related brown-pigmented Chlorobi (BGSB) are adapted to the low light levels found at deeper water depths and produce isorenieratene, the precursor of isorenieratane (18-22). Additionally, renieratane and renierapurpurane appear to arise largely from cyanobacteria, exemplified by *Synechococcus* sp. PCC 7002 (23) where they are biosynthetic precursors of an abundant pigment synechoxanthin. β-isorenieratene and β-renierapurpurin lie in the same pathway and, although traditionally ascribed to phototrophic sulfur bacteria (14, 24-26), also occur in cyanobacteria. Thus, their sources are more complex (23) and require further investigation. As an example, in this study, β-isorenieratane shows a somewhat weaker correlation with isorenieratane than it does with the monoaromatic carotenoids (Fig. S3).

Principal Component Analysis (PCA)

In order to statistically determine the contribution of environmental variability to the $\delta^{13}C_{org}$ record and to link with the mats, a principal component analysis (PCA) was undertaken, whereby different

biomarkers across a range of depths spanning the Westbury and Lilstock formations acted as variables. Ultimately, there were 8 variables selected as most representative of the microbial communities (Figures 3 and S2): sterane/hopane ratio (S/H); gammacerane index (GI); 2-methylhopane (2-MeH) index; 3-methylhopane (3-MeH) index, (renieratane+renierapurpurane)/isorenieratane [(ren+rnp)/iso]; isorenieratane/triaromatic steroids (isorenieratane/TA); (β-isorenieratane)/triaromatic steroids (β-iso/TA); and (chlorobactene+okenane)/triaromatic steroids [(chl+oke)/TA]. Accordingly, there are 8 corresponding principal components, with the first principal component (PC-1) accounting for the majority of the variance in the data. Here, samples are grouped with respect to their stratigraphic position relative to the microbial mat (below CIE, lower CIE, upper CIE, above CIE). PC-1, which is the component that accounts for the majority of variation, also displays large changes during the CIE. However, it is highly biased by a single outlier at Lilstock above the CIE. This outlier corresponds to a sedimentary interval that shows heavy bioturbation and where all biomarkers are perturbed. The corresponding stratigraphic interval at St. Audrie's Bay shows no evidence of bioturbation and no perturbation in biomarkers or PC-1, therefore PC-1 is largely driven by microbial mat growth, but is also affected by bioturbation. Comparatively, changes in PC-2 as a result of this bioturbated interval are still obvious but less apparent compared to PC-1, hence we use PC-2 to show microbial mat growth during the CIE. Note that the peak $\delta^{13}C_{org}$ minima at both St. Audrie's Bay and Lilstock coincide with the low values in PC-2 (Fig. 2; Fig. S9). Whereas Fig. 2 in the main text shows the change in PC-2, Fig. S9 shows downcore plots and cross plots of PC-1 and PC-2, and the corresponding depths and therefore $\delta^{13}C_{org}$ values. Although many of the data points centre close to zero (i.e. no significant changes in biomarkers), those data points that vary greatly from the central point, particularly on the PC-2 axis, correspond to samples within the CIE. Thus, the changes in PC-2 are driven by increases in microbial mat-related biomarkers (2-MeH, okenane, chlorobactane, isorenieratane, and gammacerane), and strongly correlate with the negative CIE, supporting our hypothesis that microbial mat formation and its associated input of isotopically light carbon to the sedimentary record is the driving factor of the CIE. Our comprehensive PCA investigation demonstrates that the greatest changes in biomarkers relating to microbial mats occur during the CIE, and that the two are correlated based on multiple proxies. In response to dramatic changes in both salinity and water depth, the formation of this microbial mat significantly changed the isotopic composition of organic matter input to the sediments and thus drove the CIE.

Sample Preparation

Rock samples were collected from sedimentary successions that crop out at St. Audrie's Bay (51.182833°, -3.286000°) and Lilstock (51.200757°, -3.176389°). Rock surfaces were removed and samples were sonicated three times at 15 minutes in the 9:1 DCM:MeOH

(Dichloromethane:Methanol) to remove any surface contamination. Samples were then powered using a Rocklabs SRM C+PB rock grinder.

Organic Carbon Isotope and Total Organic Matter Analysis

Crushed rock (<0.5g) was acidified using 2M HCl for a minimum of 12 hours to remove inorganic carbon. Additional 2M HCl was added to samples until effervescence ceased and samples were then digested for a further 12 hours. Samples were brought to a neutral pH using Milli-Q water. After centrifuging and decanting Milli-Q water, samples were freeze dried to remove the last traces of water. Elemental analysis (using a CNHS Elemental Analyser) and $\delta^{13}C$ analysis (using a Delta V Plus mass spectrometer connected with a Thermo Flush 1112 via a Conflo IV) was undertaken at the West Australian Biogeochemistry Centre, University of Western Australia under Grzegorz Skyrzypek. Details for elemental analysis can be found in Skrzypek and Paul 2006. Details for $\delta^{13}C$ analysis can be found in Skrzypek 2013.

Biomarker and Compound Specific Isotope Analysis

Rock extractions and separations were carried out at WA-OIGC, Curtin University. Organic matter compounds were extracted from powdered samples (30-150g) using a Milestone Start-E microwave extraction system in 50mL 9:1 DCM:MeOH using a temperature program of 21°C to 80°C over 10 minutes and held at 80°C for 15 minutes. Samples rich in organic matter were re-extracted to ensure all bitumen was collected. Elemental sulfur was removed using activated copper turnings. Copper turnings were washed in 9:1 DCM:MeOH to remove contamination then activated by sonicating for 30 minutes in 2M HCl and brought to a neutral pH using Milli-Q water. Total bitumens were fractionated using activated silica gel (heated to 80°C overnight) into saturate (hexane), aromatic (3:1 Hexane:DCM) and polar (9:1 DCM:MeOH) fractions. St. Audrie's Bay saturate fractions were analyzed using an Agilent 6890N gas chromatograph (GC) fitted with a DB-1 capillary column (temperature program of 4°C/min from 50°C to 325°C with a hold time of 24 minutes at 325°C), connected to a Micromass AutoSpec Ultima multiple reaction monitoring mass spectrometer (MRM-MS). The aromatic fractions from St. Audrie's Bay and the combined aliquots of saturate and aromatic fractions from Lilstock were analyzed using an Agilent 7890B GC (temperature program of 4°C/min from 40°C to 325°C with a hold time of 20.27 minutes at 325°C) connected to an Agilent 7010A triple quadrupole MS/MS. All biomarker analysis was conducted at the Summons Lab, Massachusetts Institute of Technology. Compounds were identified by comparing peak retention times and elution patterns to those in a composite oil standard provided by GeoMark Inc. Quantification was achieved using internal standards (D4 stigmastane for saturate compounds and for D10 phenanthrene aromatic compounds). All Compound Specific Isotope Analysis (CSIA) was conducted at WA-OIGC Curtin University using a Thermo Trace GC ultra (DB-1 column) coupled to a Thermo Delta V Advantage isotope ratio MS (irMS) via a GC Isolink and

Conflo IV. $\delta^{13}C$ analysis of compounds was achieved using the 44, 45, and 46 masses, integrated manually to ensure base peak separation, and run in triplicates to confirm consistent measurements. Compounds were identified using GC-MS (DB-1 column) analysis on an Agilent 6890 GC interfaced to an Agilent 5973 mass selective detector (MSD). Temperature programs for each instrument was an initial temp of 40°C for 1 min, then heated to 325°C at 3°C/min, and held at 325°C for 30 min.
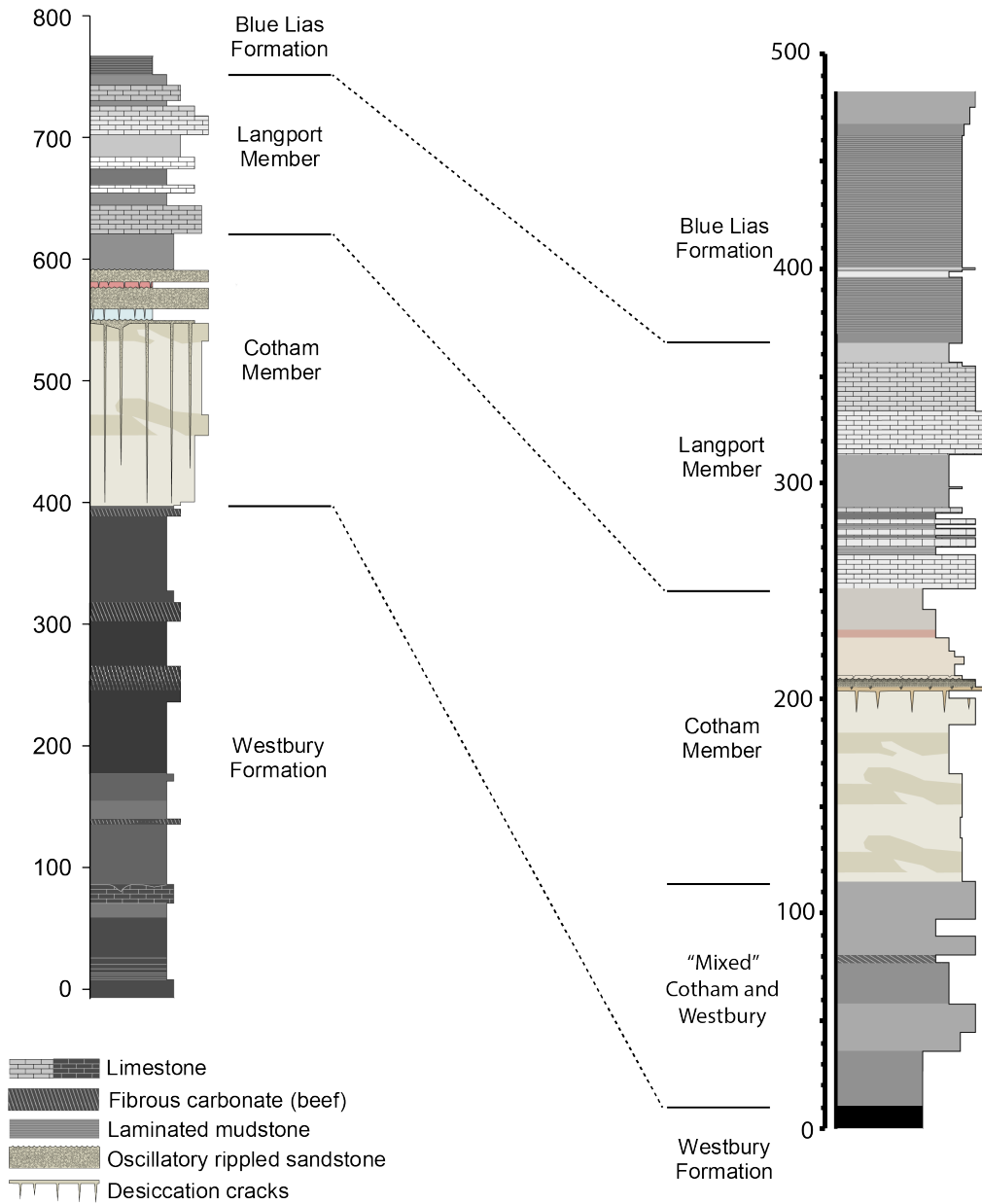
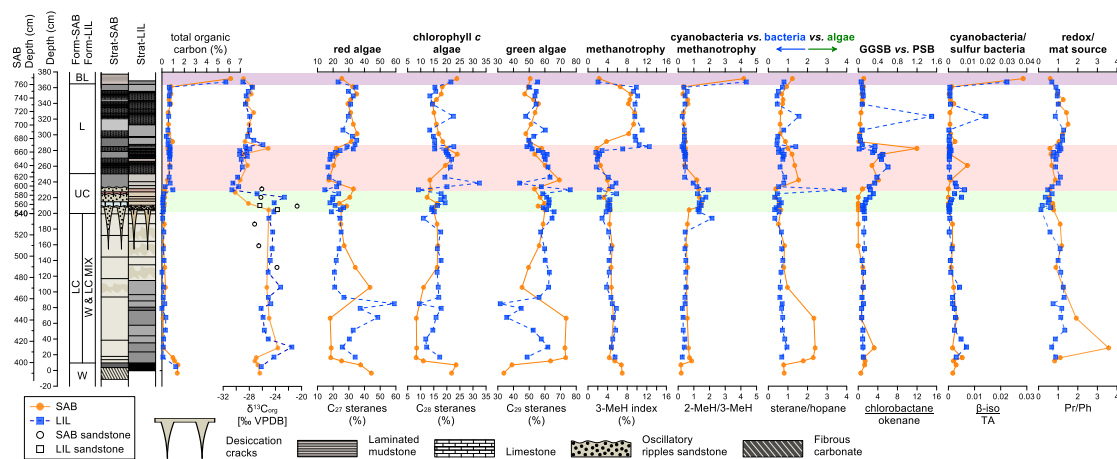**S1:** Lithological correlation between St. Audrie's Bay (left) and Lilstock (right). Depth given in cm.

Figure S2: Biomarkers indicative of ecological changes at St. Audrie's Bay (●) and Lilstock (■) relative to the $\delta^{13}C_{org}$ record. The lower CIE and upper CIE are highlighted in light green and pink, respectively, while the newly proposed extinction onset is shaded in light purple. Biomarker compounds are labeled below and their ecological or environmental indicators are given above each column.
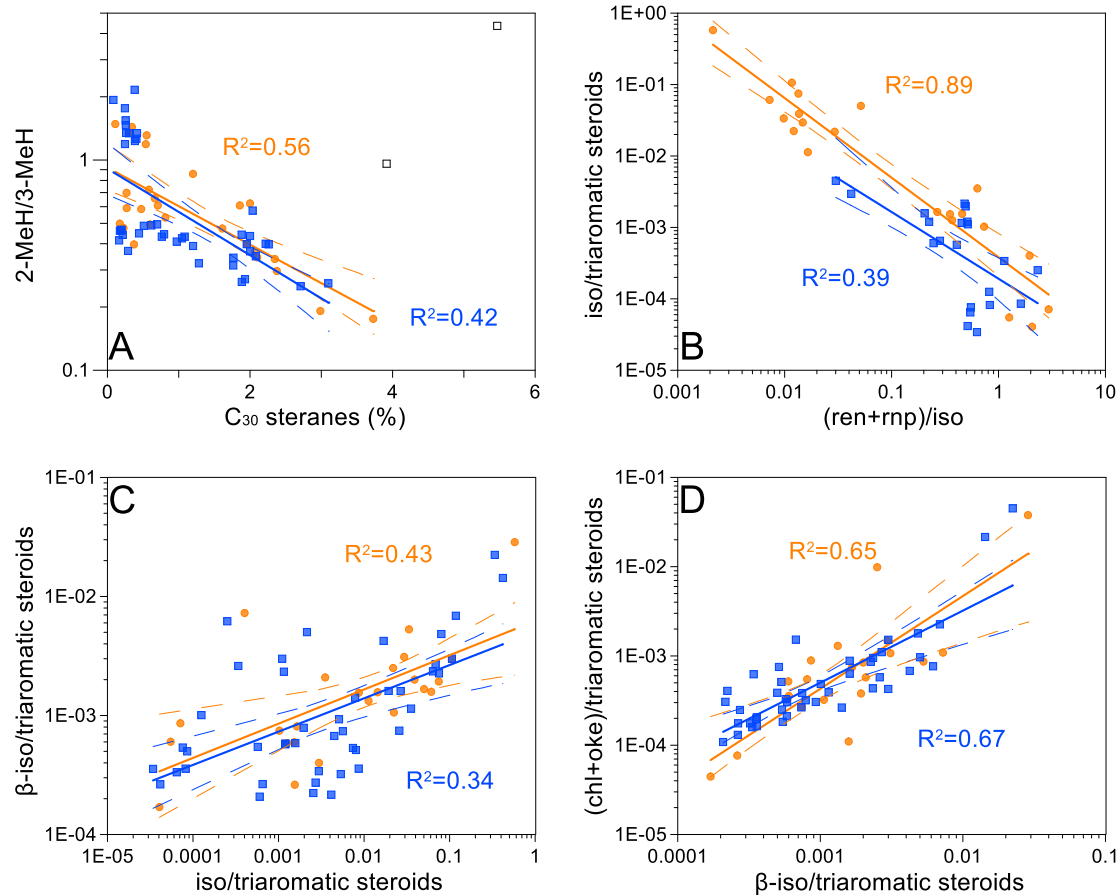
Figure S3: Correlations of selected proxies at St. Audrie's Bay (●) and Lilstock (■). Note that most axes are displayed in log scales.

Figure S4: Lilliput bivalve assemblage from St. Audrie's Bay. A, basal finely laminated Blue Lias Formation in basal pre-planorbis zone with Lilliput assemblage. Underlying strata are more massive marlstones of the uppermost Langport Member of the Lilstock Formation with abundant normal-sized bivalves. B, field photograph of bedding plane of the beds in A showing numerous very small bivalves including minute pectinoid forms comprising the Lilliput assemblage. Many have shelly material preserved. This Lilliput assemblage and characteristic facies has been observed at St. Audrie's Bay and Lilstock in Somerset and Lavernock Point, Wales. Scale bar in both A and B is 1 cm. Lilliput assemblage is restricted to the 1-cm-thick interval at the scale bar in A.
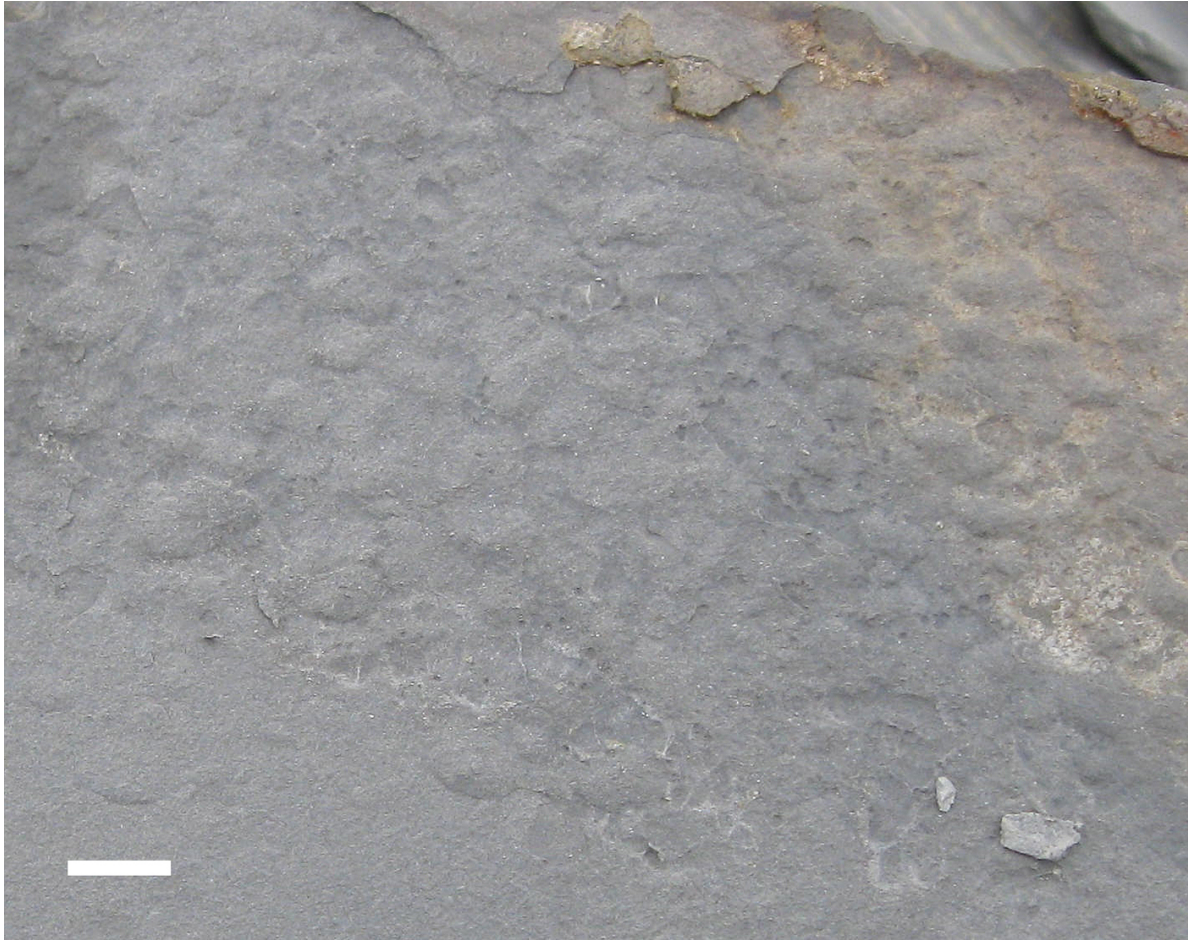
Figure S5: Bedding plane of finely laminated lower Blue Lias (pre-planorbis zone) covered with hundreds of decalcified (?) mytilid bivalves from St. Audrie's Bay. There are many such surfaces in the basal Blue Lias Formation with this example being from ~1 m above the base of the formation. Scale bar is 1 cm.
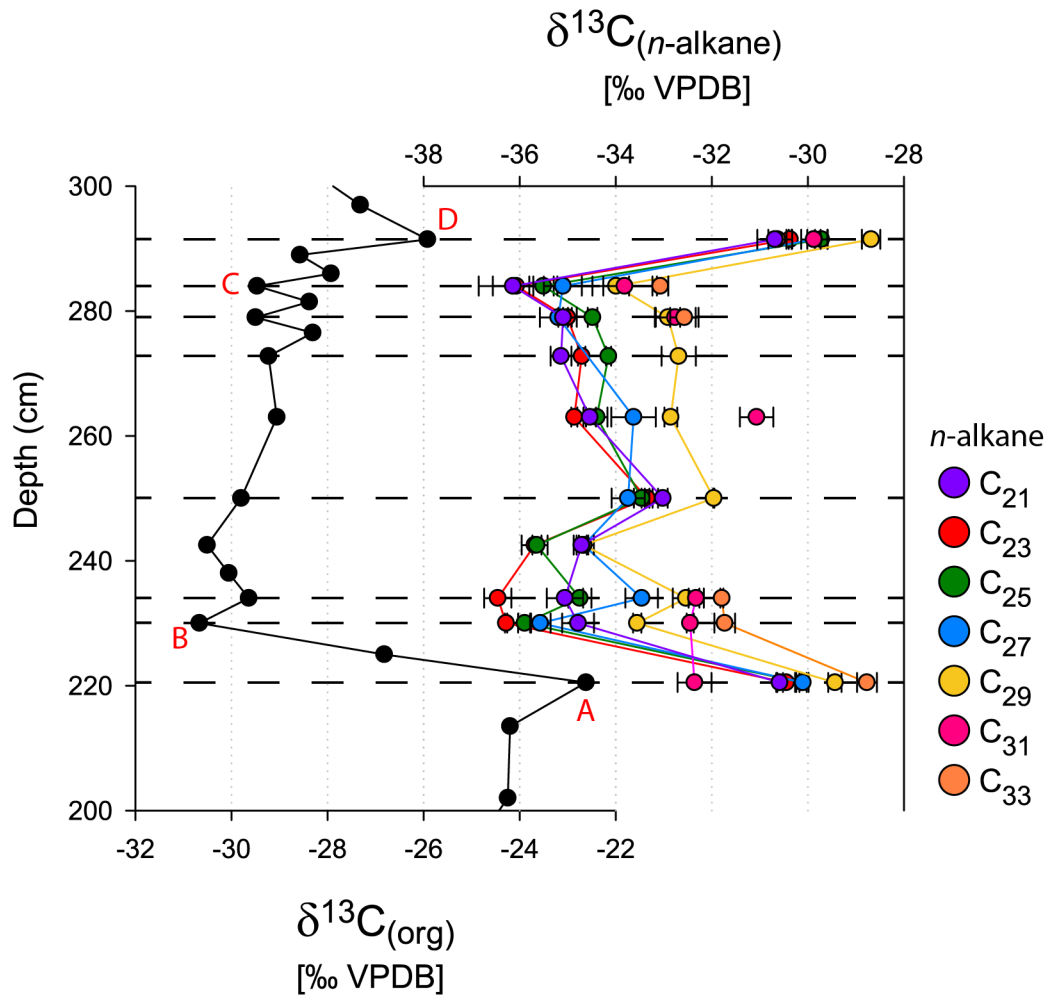
Compound specific carbon isotope analysis (CSIA) of odd chain *n*-alkanes between C$_{21}$ and C$_{33}$ at Lilstock. A to B marks the CIE onset, and C to D marks the termination. Absolute magnitudes are given in Table S1.
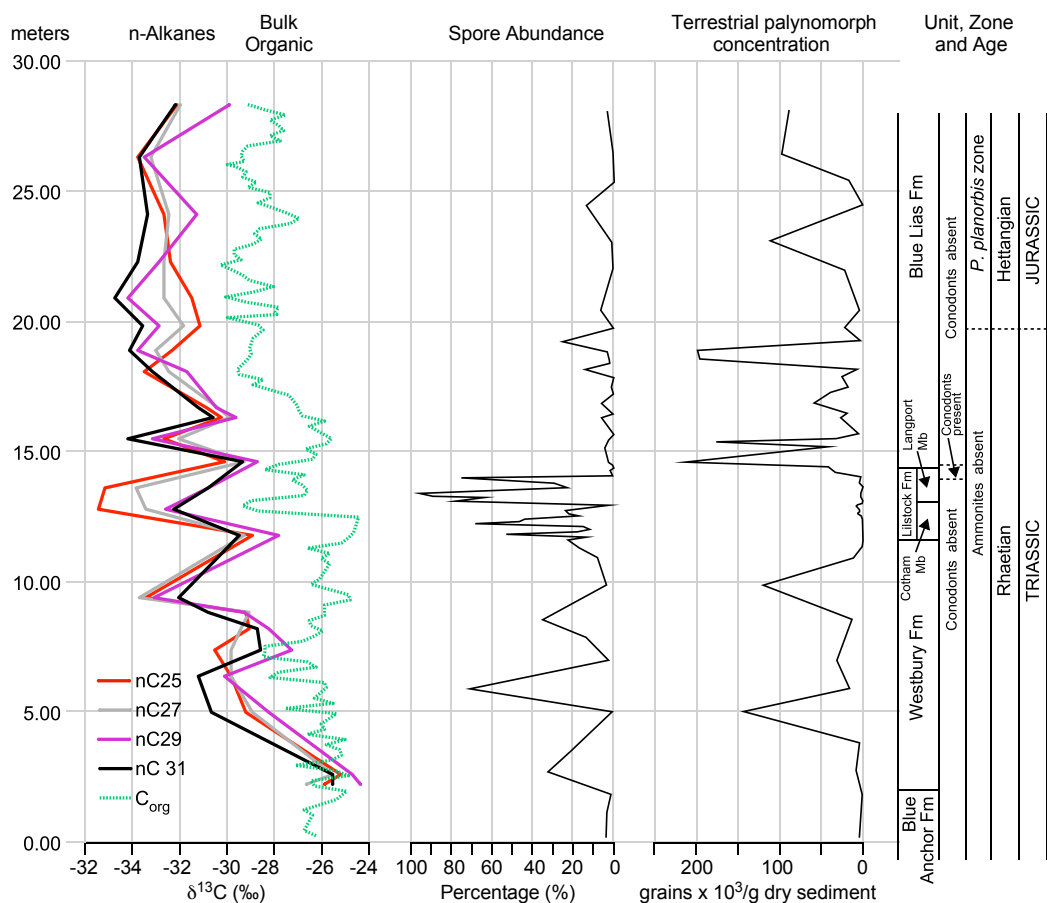
Figure S7: Compound specific carbon isotopic composition (CSIA) of *n*-alkanes compared to that of bulk organic carbon, spore and total terrestrial palynomorph concentration. Note cyclical behavior of *n*-alkanes that cannot directly reflect light carbon input into the atmosphere and its overall correspondence to terrestrial palynomorphs. TOC is very low in the Cotham Member so that spores disproportionally contribute to the organic matter composition. Data for *n*-alkanes are from reference (27); $\delta^{13}C_{org}$ and unit, zone, and age are from reference (28), spore abundance and terrestrial palynomorph concentration are from reference (29).
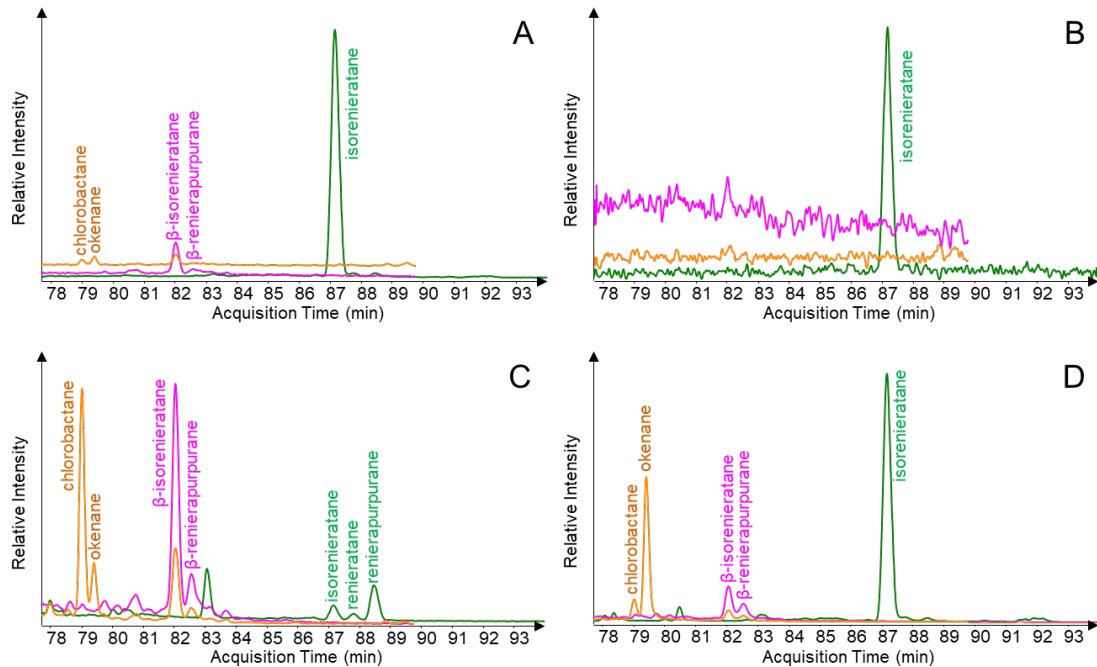
Figure S8: Aromatic carotenoid GC-MRM-MS profiles during the pre-CIE (A; sample No. 3), lower CIE (B; No. 9), upper CIE (C; No. 15), and post-CIE (D; sample No. 19) during the regression-transgression events at the St. Audrie's Bay section. MRM transitions for the C_{40} carotenoids are 554 → 134 (okenane and chlorobactane; orange), 552 → 134 (β-isorenieratane and β-renierapurpurane; purple), and 546→134 (isorenieratane, renieratane and renierapurpurane; green). Note that the origins of some carotenoids such as β-renierapurpurane remain uncertain and are not considered further in this study.
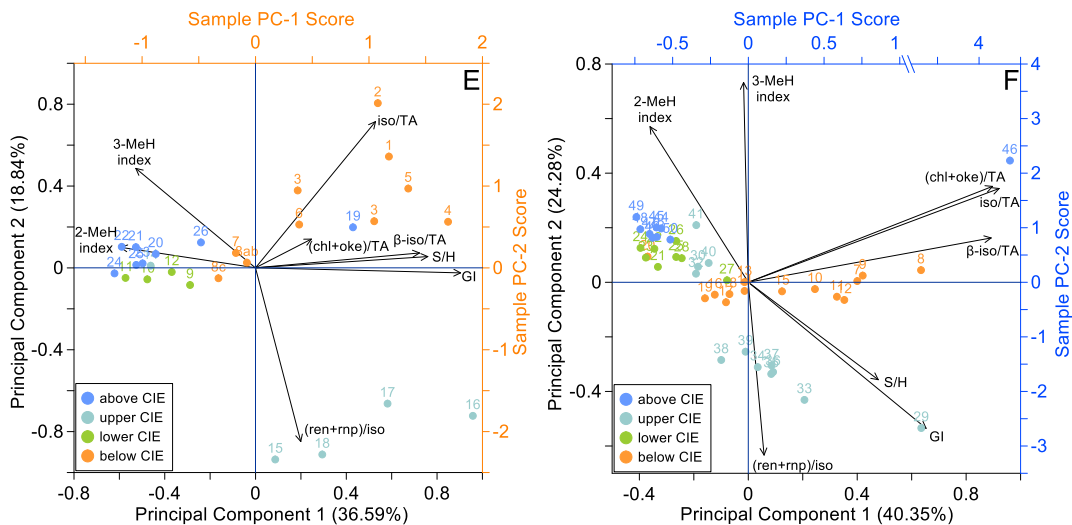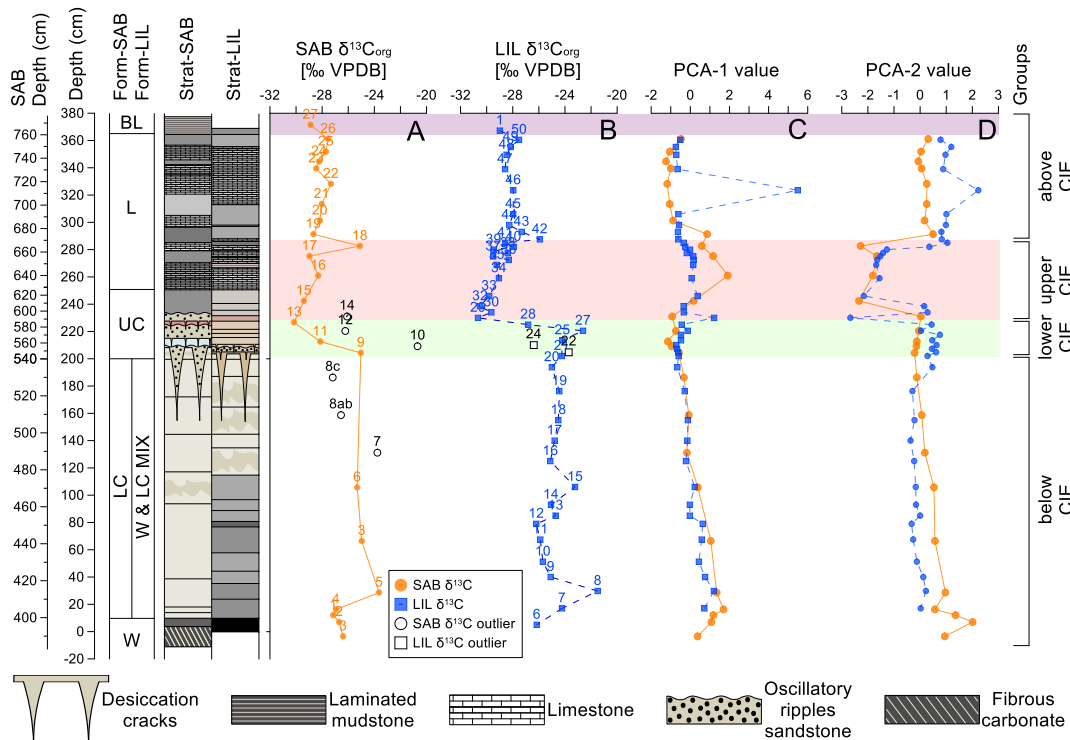
Figure S9: A-B): Sample number of St. Audrie's Bay (orange; A) and Lilstock (blue; B) at their $\delta^{13}C_{org}$ position. Black sample numbers indicate removed sandstone samples. C-D): Principal component (PC) 1 and 2 values for St. Audrie's Bay (C) and Lilstock (D) samples based on principal component analysis (PCA). Shaded light green and pink areas indicate the CIE. Group intervals are given as "below CIE", "lower CIE", "upper CIE", and "above CIE". E-F): PC-1 vs. PC-2 plots for St. Audrie's Bay (E) and Lilstock (F) with samples grouped according to A-D. As shown, the grouped "lower CIE" and "upper CIE" show most lateral variability in second principal component (PC-2). Whilst PC-2 shows the largest variation associated with the CIE, PC-1 also records variability driven by microbial mat formation but is affected by one outlier above the CIE related to a heavy bioturbated interval.

Table S1: $\delta^{13}C_{org}$ and compound specific isotopic shifts of pristane, phytane, C_{18} *n*-alkane and odd-numbered *n*-alkanes in the range C_{17-33} during the onset and termination of the CIE. SAB – St. Audrie's Bay; L – Lilstock. Mid to long chain *n*-alkane profiles, and A to B and C to D profiles are given in Fig. S6.

	Section	CIE start (A→B)	CIE end (C→D)
Pristane (‰)	SAB	-2.0	-0.5
	LIL	-2.1	0.4
Phytane (‰)	SAB	-5.1	-0.6
	LIL	-2.5	0.5
C_{17} (‰)	LIL	-1.8	2.8
C_{18} (‰)	LIL	-2.2	3.0
C_{19} (‰)	LIL	-2.7	3.2
C_{21} (‰)	LIL	-4.2	5.5
C_{23} (‰)	LIL	-6.0	5.7
C_{25} (‰)	LIL	-4.6	5.8
C_{27} (‰)	LIL	-5.5	5.2
C_{29} (‰)	LIL	-4.1	5.3
C_{31} (‰)	LIL	-0.1	3.9
C_{33} (‰)	LIL	-3.0	2.4
$\delta^{13}C_{org}$ (‰)	SAB	-5.1	3.9
	LIL	-8.1	3.6

Table S2: Biomarkers, their equations, and the *m/z* transitions monitored. TA: triaromatic steroids.

Index/Biomarker	Calculation	MRM
Steranes		
C$_{27}$ Sterane Index (%) (all)	$\dfrac{\sum C_{27 \text{ steranes}}}{\sum C_{27-29 \text{ steranes}}} \times 100$	$372 \rightarrow 217$
C$_{28}$ Sterane Index (%) (all)	$\dfrac{\sum C_{28 \text{ steranes}}}{\sum C_{27-29 \text{ steranes}}} \times 100$	$386 \rightarrow 217$
C$_{29}$ Sterane Index (%) (all)	$\dfrac{\sum C_{29 \text{ steranes}}}{\sum C_{27-29 \text{ steranes}}} \times 100$	$400 \rightarrow 217$
C$_{30}$ Sterane Index (%) (diasteranes)	$\dfrac{\sum C_{30 \text{ steranes}}}{\sum C_{27-30 \text{ steranes}}} \times 100$	$414 \rightarrow 217$
Hopanes		
C$_{30\text{-}32}$ 2α-methylhopane Index (%)	$\dfrac{C_{30-32} 2\alpha \text{ methylhopane}}{C_{30-32} \alpha\beta \text{ hopane}} \times 100$	$426 \rightarrow 205$
C$_{30\text{-}32}$ 3β-methylhopane Index (%)	$\dfrac{C_{30-32} 3\beta \text{ methylhopane}}{C_{30-32} \alpha\beta \text{ hopane}} \times 100$	$426 \rightarrow 205$
Gammacerane Index (%)	$\dfrac{\text{gammacerane}}{C_{30} \alpha\beta \text{ hopane} + \text{gammacerane}} \times 100$	$412 \rightarrow 191$
C$_{40}$ Carotenoids		
Okenane	okenane/C$_{26\text{-}28}$ TA	$554 \rightarrow 134$
Chlorobactane	chlorobactane/C$_{26\text{-}28}$ TA	$554 \rightarrow 134$
β-Isorenieratane	β-isorenieratane/C$_{26\text{-}28}$ TA	$552 \rightarrow 134$
Isorenieratane	isorenieratane/C$_{26\text{-}28}$ TA	$546 \rightarrow 134$
Renieratane	renieratane/C$_{26\text{-}28}$ TA	$546 \rightarrow 134$
Renierapurpurane	renierapurpurane/C$_{26\text{-}28}$ TA	$546 \rightarrow 134$
Others		
Pristane to Phytane Ratio	$\dfrac{\text{pristane}}{\text{phytane}}$	Identified using GC-MS
Hopanes (regular) Vs. Steranes (regular) Index (%)	$\dfrac{C_{27-29} \text{ steranes (all)}}{C_{27-35} \text{ hopanes (all)}}$	See above

Supplementary Information References

1. R. B. Kodner, A. Pearson, R. E. Summons, A. H. Knoll, Sterols in red and green algae: quantification, phylogeny, and relevance for the interpretation of geologic steranes. *Geobiology* **6**, 411-420 (2008).
2. G. W. Patterson, The distribution of sterols in algae. *Lipids* **6**, 120-127 (1971).
3. A. H. Kasprak *et al.*, Episodic photic zone euxinia in the northeastern Panthalassic Ocean during the end-Triassic extinction. *Geology* **43**, 307-310 (2015).
4. J. K. Volkman *et al.*, Microalgal biomarkers: a review of recent research developments. *Organic Geochemistry* **29**, 1163-1179 (1998).
5. J. K. Volkman, S. M. Barrett, G. A. Dunstan, S. Jeffrey, Sterol biomarkers for microalgae from the green algal class Prasinophyceae. *Organic Geochemistry* **21**, 1211-1218 (1994).
6. K. E. Peters, K. E. Peters, C. C. Walters, J. Moldowan, *The biomarker guide* (Cambridge University Press, 2005), vol. 1.
7. R. E. Summons, L. L. Jahnke, J. M. Hope, G. A. Logan, 2-Methylhopanoids as biomarkers for cyanobacterial oxygenic photosynthesis. *Nature* **400**, 554-557 (1999).
8. S. E. Rashby, A. L. Sessions, R. E. Summons, D. K. Newman, Biosynthesis of 2-methylbacteriohopanepolyols by an anoxygenic phototroph. *Proceedings of the National Academy of Sciences* **104**, 15099-15104 (2007).
9. J. Ricci, A. Michel, D. Newman, Phylogenetic analysis of HpnP reveals the origin of 2‐methylhopanoid production in Alphaproteobacteria. *Geobiology* **13**, 267-277 (2015).
10. M. Rohmer, P. Bouvier-Nave, G. Ourisson, Distribution of hopanoid triterpenes in prokaryotes. *Microbiology* **130**, 1137-1150 (1984).
11. M. Zundel, M. Rohmer, Hopanoids of the methylotrophic bacteria Methylococcus capsulatus and Methylomonas sp. as possible precursors of C29 and C30 hopanoid chemical fossils. *FEMS microbiology letters* **28**, 61-64 (1985).
12. M. Zundel, M. Rohmer, Prokaryotic triterpenoids: 3. The biosynthesis of 2β‐methylhopanoids and 3β‐methylhopanoids of Methylobacterium organophilum and Acetobacter pasteurianus ssp. pasteurianus. *European Journal of Biochemistry* **150**, 35-39 (1985).
13. J. S. Sinninghe Damsté *et al.*, Evidence for gammacerane as an indicator of water column stratification. *Geochimica et Cosmochimica Acta* **59**, 1895-1900 (1995).
14. J. J. Brocks, P. Schaeffer, Okenane, a biomarker for purple sulfur bacteria (Chromatiaceae), and other new carotenoid derivatives from the 1640 Ma Barney Creek Formation. *Geochimica et Cosmochimica Acta* **72**, 1396-1414 (2008).
15. P. Schaeffer, P. Adam, P. Wehrung, P. Albrecht, Novel aromatic carotenoid derivatives from sulfur photosynthetic bacteria in sediments. *Tetrahedron Letters* **38**, 8413-8416 (1997).
16. J. Overmann, J. T. Beatty, K. J. Hall, N. Pfennig, T. G. Northcote, Characterization of a dense, purple sulfur bacterial layer in a meromictic salt lake. *Limnology and Oceanography* **36**, 846-859 (1991).
17. K. Grice, S. Schouten, K. E. Peters, J. S. S. Damsté, Molecular isotopic characterisation of hydrocarbon biomarkers in Palaeocene–Eocene evaporitic, lacustrine source rocks from the Jianghan Basin, China. *Organic Geochemistry* **29**, 1745-1764 (1998).
18. K. Grice, P. Schaeffer, L. Schwark, J. R. Maxwell, Molecular indicators of palaeoenvironmental conditions in an immature Permian shale (Kupferschiefer, Lower

Rhine Basin, north-west Germany) from free and S-bound lipids. *Organic Geochemistry* **25**, 131-147 (1996).

19. S. L. Jensen, Bacterial carotenoids. *Acta chem. scand* **19** (1965).

20. R. E. Summons, T. G. Powell, Chlorobiaceae in Palaeozoic seas revealed by biological markers, isotopes and geology. *Nature* **319**, 763-765 (1986).

21. J. Overmann (2008) Ecology of phototrophic sulfur bacteria. Sulfur Metabolism in Phototrophic Organisms: Advances in Photosynthesis and Respiration, Vol. 27 (Hell R, Dahl C, Knaff DB & Leustek T, eds). (Springer, New York).

22. J. Overmann, H. Cypionka, N. Pfennig, An extremely low‑light adapted phototrophic sulfur bacterium from the Black Sea. *Limnology and oceanography* **37**, 150-155 (1992).

23. X. Cui *et al.*, Niche expansion for phototrophic sulfur bacteria at the Proterozoic–Phanerozoic transition. *Proceedings of the National Academy of Sciences* **117**, 17599-17606 (2020).

24. A. Behrens, P. Schaeffer, S. Bernasconi, P. Albrecht, Mono-and bicyclic squalene derivatives as potential proxies for anaerobic photosynthesis in lacustrine sulfur-rich sediments. *Geochimica et Cosmochimica Acta* **64**, 3327-3336 (2000).

25. N.-U. Frigaard, J. A. Maresca, C. E. Yunker, A. D. Jones, D. A. Bryant, Genetic manipulation of carotenoid biosynthesis in the green sulfur bacterium Chlorobium tepidum. *Journal of bacteriology* **186**, 5210-5220 (2004).

26. A. Roussel, X. Cui, R. E. Summons, Biomarker stratigraphy in the Athel Trough of the South Oman Salt Basin at the Ediacaran‑Cambrian Boundary. *Geobiology*.

27. J. H. Whiteside, P. E. Olsen, T. Eglinton, M. E. Brookfield, R. N. Sambrotto, Compound-specific carbon isotopes from Earth's largest flood basalt eruptions directly linked to the end-Triassic mass extinction. *Proceedings of the National Academy of Sciences* **107**, 6721-6725 (2010).

28. S. P. Hesselbo, S. A. Robinson, F. Surlyk, S. Piasecki, Terrestrial and marine extinction at the Triassic-Jurassic boundary synchronized with major carbon-cycle perturbation: A link to initiation of massive volcanism? *Geology* **30**, 251-254 (2002).

29. N. R. Bonis, M. Ruhl, W. M. Kürschner, Milankovitch-scale palynological turnover across the Triassic–Jurassic transition at St. Audrie's Bay, SW UK. *Journal of the Geological Society* **167**, 877-888 (2010).